

Cross Section Measurements of Charged Pion Photoproduction in Hydrogen and Deuterium from 1.1 to 5.5 GeV

L. Y. Zhu,¹ J. Arrington,² T. Averett,^{3,4} E. Beise,⁵ J. Calarco,⁶ T. Chang,⁷ J. P. Chen,⁴ E. Chudakov,⁴ M. Coman,⁸ B. Clasie,¹ C. Crawford,¹ S. Dieterich,⁹ F. Dohrmann,² D. Dutta,¹ K. Fissum,¹⁰ S. Frullani,¹¹ H. Gao,^{1,12} R. Gilman,^{4,9} C. Glashauser,⁹ J. Gomez,⁴ K. Hafidi,² O. Hansen,⁴ D. W. Higinbotham,¹ R. J. Holt,² C. W. de Jager,⁴ X. Jiang,⁹ E. Kinney,¹³ K. Kramer,³ G. Kumbartzki,⁹ J. LeRose,⁴ N. Liyanage,⁴ D. Mack,⁴ P. Markowitz,⁸ K. McCormick,⁹ D. Meekins,⁴ Z.-E. Meziani,¹⁴ R. Michaels,⁴ J. Mitchell,⁴ S. Nanda,⁴ D. Potterveld,² R. Ransome,⁹ P. E. Reimer,² B. Reitz,⁴ A. Saha,⁴ E. C. Schulte,^{2,7} J. Seely,¹ S. Širca,¹ S. Strauch,⁹ V. Sulkosky,³ B. Vlahovic,¹⁵ L. B. Weinstein,¹⁶ K. Wijesooriya,² C. Williamson,¹ B. Wojtsekhowski,⁴ H. Xiang,¹ F. Xiong,¹ W. Xu,¹ J. Zeng,¹⁷ and X. Zheng¹

(Jefferson Lab Hall A Collaboration and Jefferson Lab E94-104 Collaboration)

¹Massachusetts Institute of Technology, Cambridge, MA 02139, USA

²Argonne National Laboratory, Argonne, IL 60439, USA

³College of William and Mary, Williamsburg, VA 23185, USA

⁴Thomas Jefferson National Accelerator Facility, Newport News, VA 23606, USA

⁵University of Maryland, College Park, MD 20742, USA

⁶University of New Hampshire, Durham, NH 03824, USA

⁷University of Illinois, Urbana, IL 61801, USA

⁸Florida International University, Miami, FL 33199, USA

⁹Rutgers University, New Brunswick, NJ 08903, USA

¹⁰Lund University, S-221 00 Lund, Sweden

¹¹INFN/Sezione Sanita, 00161 Roma, Italy

¹²Duke University, Durham, NC 27708, USA

¹³University of Colorado, Boulder, CO 80302, USA

¹⁴Temple University, Philadelphia, PA 19122, USA

¹⁵North Carolina Central University, Durham, NC 27707, USA

¹⁶Old Dominion University, Norfolk, VA 23529, USA

¹⁷University of Georgia, Athens, GA 30601, USA

(Dated: August 20, 2019)

The differential cross section for the $\gamma n \rightarrow \pi^- p$ and the $\gamma p \rightarrow \pi^+ n$ processes were measured at Jefferson Lab. The photon energies ranged from 1.1 to 5.5 GeV, corresponding to center-of-mass energies from 1.7 to 3.4 GeV. The pion center-of-mass angles varied from 50° to 110° . The π^- and π^+ photoproduction data both exhibit a global scaling behavior at high energies and high transverse momenta, consistent with the constituent counting rule prediction and the existing π^+ data. The data suggest possible substructure of the scaling behavior, which might be oscillations around the scaling value. The data show an enhancement in the scaled cross section at center-of-mass energy near 2.2 GeV. The differential cross section ratios $\frac{d\sigma/dt(\gamma n \rightarrow \pi^- p)}{d\sigma/dt(\gamma p \rightarrow \pi^+ n)}$ at high energies and high transverse momenta can be described by calculations based on one-hard-gluon-exchange diagrams.

PACS numbers: 13.60.Le, 24.85.+p, 25.10.+s, 25.20.-x

I. INTRODUCTION

Quantum ChromoDynamics (QCD), a fundamental theory for describing the strong interaction, is not amenable to analytical solutions in the nonperturbative region. Some dynamical models must be developed. Meson-exchange models in terms of the nucleon-meson degrees of freedom describe nuclear physics data well at low energy, and perturbative QCD (pQCD) in terms of the quark-gluon degrees of freedom succeeds in explaining many measurements at high energy. But little is known about the transition between these two regions. Testing the constituent counting rule for the exclusive reactions is one way to study the transition of the degrees of freedom.

The constituent counting rule establishes a direct con-

nection between the quark-gluon degrees of freedom and the energy dependence of the differential cross section for exclusive processes at fixed center-of-mass angles. This rule was first derived from simple dimensional counting [1, 2, 3] and was later confirmed in a short-distance pQCD approach [4]. It is consistent with many exclusive measurements [5, 6, 7, 8, 9]. However, there are still many puzzles. This rule begins to agree with experimental data at energies as low as 1 GeV [7, 8], whereas pQCD is not expected to be valid at such low energies. The hadron helicity conservation rule [10], another outcome of the same short-distance pQCD framework, does not agree with data in the same energy and momentum transfer region [11, 12]. There are a few anomalies beyond the constituent counting rule in the extensively studied pp scattering process [13, 14, 15]. Recently, the

parton orbital angular momentum has been found to play a non-negligible role in the exclusive reactions, which may explain hadron helicity nonconservation and other polarization measurements [16, 17].

Single pion photoproduction, $\gamma N \rightarrow \pi N$, is a relatively simple process for studying the strong interaction. It has larger cross sections at high energy than other exclusive channels due to its slower decrease with energy, i.e. $d\sigma/dt \sim s^{-7}$. One can also form the differential cross section ratio $\frac{d\sigma/dt(\gamma n \rightarrow \pi^- p)}{d\sigma/dt(\gamma p \rightarrow \pi^+ n)}$. The ratio is amenable to theoretical predictions since many factors may cancel out in leading order.

This paper focuses on extracting the differential cross sections for the single charged pion photoproduction processes, $\gamma p \rightarrow \pi^+ n$ and $\gamma n \rightarrow \pi^- p$. This is one major goal of experiment E94-104 [18] carried out at Jefferson Lab (JLab). The photon beam energy ranged from 1.1 to 5.5 GeV. The pion center-of-mass angles varied from 50° to 110° . The results at 90° have already been published [19], which are also updated in this paper. The experiment E94-104 also measured π^- photoproduction with a helium target, providing the first nuclear transparency data for this process [20].

This paper is organized as follows. Section II introduces the theoretical and experimental background for JLab experiment E94-104. Section III describes this experiment at JLab Hall A. Section IV presents the data analysis procedure to extract the differential cross sections. Section V discusses the results. Section VI and VII are outlook and acknowledgments.

II. THEORETICAL AND EXPERIMENTAL BACKGROUND

The constituent counting rule is also called the dimensional scaling rule. It states that

$$(d\sigma/dt)_{AB \rightarrow CD} \sim s^{-(n-2)} f(\theta_{c.m.}) \quad (1)$$

for an exclusive two-body reaction $AB \rightarrow CD$ when $s \rightarrow \infty$. Here s and t are the Mandelstam variables and n is the total number of elementary fields (quarks, leptons or photons) which carry finite fractions of particle momentum. It predicts a scaling behavior of the differential cross sections at fixed center-of-mass angle $\theta_{c.m.}$ and large s . For example $(d\sigma/dt)_{pp \rightarrow pp} \sim s^{-10}$, $(d\sigma/dt)_{\pi p \rightarrow \pi p} \sim s^{-8}$, $(d\sigma/dt)_{\gamma d \rightarrow pn} \sim s^{-11}$ and $(d\sigma/dt)_{\gamma N \rightarrow \pi N} \sim s^{-7}$. The constituent counting rule implies something of fundamental importance: the quark has not only a mathematical existence, giving current algebra, Bjorken scaling and the hadron spectrum, but a dynamical existence as well [2].

The constituent counting rule was originally derived from simple dimensional counting by Brodsky and Farrar [1], and simultaneously by Matveev *et al.* [3] in 1973. Brodsky and Farrar also examined the required conditions for the simple dimensional derivation:

(a) the effective replacement of the composite hadron by constituents carrying finite fractions of the hadron momentum,

(b) the absence of any mass scale in the amplitude or binding corrections.

They showed that both condition (a) and (b) are natural features of renormalizable field theories, with certain dynamical assumptions concerning the nature of the wave function, the absence of infrared effects, and the accumulation of logarithms [2].

Later in 1980, Lepage and Brodsky showed that the constituent counting rule can be reproduced within a short-distance pQCD approach [4], up to calculable powers of the strong coupling constant. The energy dependence of the strong coupling constant is small at high energy, and some recent τ decay data also suggest the freezing of the coupling constant at low energy [21].

Another outcome of this approach is hadron helicity conservation [10]:

$$h_A + h_B = h_C + h_D, \quad (2)$$

which leads to strong correlations between the final state helicities. The above results came from the calculation of an enormous number of connected tree diagrams for hard subprocesses without considering the parton orbital angular momentum, while the soft subprocesses, such as Landshoff diagrams [22] were suppressed in leading order for example due to gluon radiation.

The scaling behavior of the differential cross section predicted by the constituent counting rule can also be described by string theory [23] and other phenomenological models. For the deuteron photodisintegration process as an example, the Quark-Gluon String model (QGS) [24], the Reduced Nuclear Amplitudes (RNA) [25], the Asymptotic Meson Exchange Calculation (AMEC) [26] and the Hard Rescattering Mechanism (HRM) [27] can all describe the scaling behavior at $\theta_{c.m.} = 90^\circ$ [7, 8, 28]. In particular, QGS and HRM are in fair agreement with the asymmetric angular distribution of the deuteron photodisintegration data [8, 28, 29].

On the experimental side, the constituent counting rule is consistent with data for many exclusive processes, such as pp elastic scattering [5], hadron-hadron elastic scattering [6] and deuteron photodisintegration [7, 8, 28]. The fitted power of $\frac{1}{s}$ from the pp elastic scattering data with $s > 15 \text{ GeV}^2$ and $|t| > 2.5 \text{ GeV}^2$ is equal to 9.7 ± 0.5 [5], consistent with 10 as predicted by the constituent counting rule. Eight meson-baryon and two baryon-baryon exclusive reactions at $\theta_{c.m.} = 90^\circ$ were measured at the AGS (the Alternate Gradient Synchrotron at BNL) with beam momenta of 5.9 GeV/c and 9.9 GeV/c. The fitted powers of $\frac{1}{s}$ are also consistent with the constituent counting rule predictions, i.e. 8 for the meson-baryon reactions and 10 for the baryon-baryon reactions, except for one reaction: $\pi^- p \rightarrow \pi^+ \Delta^-$ [6]. Deuteron photodisintegration is another process that exhibits scaling behavior of the differential cross sections [7, 8, 28]. The onset of

scaling in photon energy for deuteron photodisintegration depends greatly on the center-of-mass angles. The corresponding threshold of the proton transverse momentum, $P_T = \sqrt{\frac{1}{2}M_d E_\gamma \sin^2 \theta_{c.m.}}$, is less than 1.3 GeV/c for the proton angle between 30° and 150° [8].

Despite the theoretical and experimental support for the constituent counting rule, there remain some puzzles and anomalies. First of all, it is surprising to see the onset of scaling as low as 1 GeV, such as in the photodisintegration data at $\theta_{c.m.} = 90^\circ$ [7, 8]. The applicability of pQCD to exclusive processes remains controversial in the GeV region. The pQCD calculation fails to predict the magnitude of some fundamental quantities, such as the proton magnetic form factor G_M^p with Q^2 up to 30 (GeV/c)^2 [30]. Hadron helicity conservation, another consequence of pQCD (this statement is currently under debate [31]), tends not to agree with polarization measurements, such as those from JLab for the photodisintegration process $d(\vec{\gamma}, \vec{p})n$ up to 2.4 GeV [11] and neutral pion photoproduction $p(\vec{\gamma}, \vec{p})\pi^0$ up to 4.1 GeV [12]. Although contributions from nonzero parton orbital angular momentum are power suppressed as shown by Lepage and Brodsky [4], they could break hadron helicity conservation rule [16]. Orbital angular momentum could also lead to asymptotic scaling of the proton form factor ratio: $F_2(Q^2)/F_1(Q^2) \sim (\log^2 Q^2/\Lambda^2)/Q^2$ with $0.2 \text{ GeV} \leq \Lambda \leq 0.4 \text{ GeV}$ based on an explicit pQCD calculation [17] or $F_2(Q^2)/F_1(Q^2) \sim 1/\sqrt{Q^2}$ [31, 32] that agrees with the JLab proton form factor data [33]. A recent nonperturbative analysis [34] of the hadronic form factors based on light-front wave functions also describes the JLab proton form factor data [33] well.

Furthermore, several striking anomalies have been observed in pp scattering. One is the very large spin-spin correlation. The ratio of $(d\sigma/dt)_{\uparrow\uparrow}/(d\sigma/dt)_{\uparrow\downarrow}$ with spin normal to the scattering plane can reach 4 in pp elastic scattering at $\theta_{c.m.} = 90^\circ$ [13]. Next is the oscillation of the differential cross section $d\sigma/dt$ around the scaling value in pp elastic scattering [14]. The third is the anomalous energy dependence of nuclear transparency of the $A(p, 2p)$ process [15].

There exist different theoretical attempts to describe the anomalies. One example is the interference between two types of subprocesses, the short-distance hard subprocesses and the long-distance soft (Landshoff) subprocesses [35]. Another example is the interference between the pQCD background and two $J = L = S = 1, B = 2$ resonance structures associated with the strangeness and charm production thresholds [36].

Recently, more mechanisms were under discussion that can lead to the deviation from the scaling. For example, the generalized constituent counting rule [37, 38] including the parton orbital angular momentum and the restricted locality of quark-hadron duality [40].

Including the nonzero parton orbital angular momentum may change the expression of the constituent counting rule. Based on a hadronic light-cone wave function

involving parton orbital angular momentum, which has been used to describe the JLab proton form factor data, a generalized constituent counting rule [37] can be derived for hard exclusive processes by counting the soft mass dimensions of scattering amplitudes. This generalized constituent counting rule with parton orbital angular momentum dependence can be also derived [38] in a non-perturbative method, which does not rely on pQCD. According to the generalized constituent counting rule, the fixed-angle scattering cross section behaves like

$$\Delta\sigma \sim s^{-1-\sum_H (n_H+|l_{zH}|-1)}, \quad (3)$$

for the exclusive reaction $A + B \rightarrow C + D + \dots$, where n_H is the number of elementary fields in involved hadron H and $\Delta\sigma$ contains only angular variables. For parton orbital angular momentum $l_{zH} = 0$, this is just the traditional constituent counting rule. As a result, the helicity-flip amplitudes for the $pp \rightarrow pp$ process were predicted to scale as $s^{-9/2}$ with $\sum_H |l_{zH}| = 1$ or s^{-5} with $\sum_H |l_{zH}| = 2$, while the helicity conserving amplitudes were known to scale as s^{-4} . The interference between amplitudes with different helicity changes offers a new mechanism to explain the spin-spin correlation and oscillation around the scaling value in pp scattering [39]. This can also lead to the deviation from the traditional constituent counting rule for other exclusive processes, such as photoproduction of charged pions that is discussed in this paper.

Therefore, a detailed investigation of the scaling behavior may enable a test of the generalized counting rule, though a more rigorous test should come from the polarization measurements, which would allow the separation of amplitudes with different helicity changes.

The deviation from the constituent counting rule for exclusive processes may also be due to the breakdown of the locality of quark-hadron duality [40]. Quark-hadron duality is an empirical property of the data discovered by Bloom and Gilman before the advent of QCD [41]. The production of resonances at lower energies and momentum transfers averages smoothly around the scaling curve measured at large momentum transfers. The sum over resonances can be related to the scaling behavior as a result of destructive interference. This is rather local at high energy due to the high density of the overlapping resonances, which is called the locality of quark-hadron duality. But the local degeneracy may not be reached at energies of a few GeV, which leads to the restricted locality of quark-hadron duality. The restricted locality may cause oscillations around the scaling value above the resonance region when different partial waves are not canceled locally.

The exclusive charged pion ratio of $\frac{d\sigma/dt(\gamma n \rightarrow \pi^- p)}{d\sigma/dt(\gamma p \rightarrow \pi^+ n)}$ can be estimated based on the one-hard-gluon-exchange Feynman diagrams [42, 43]. In Huang *et al.*'s approach [42], the helicity amplitude for the photoproduction of a meson was assumed to factorize into the parton-level subprocess amplitude and the nucleon form factors. Evaluating the four Feynman diagrams in Figure 1 gives

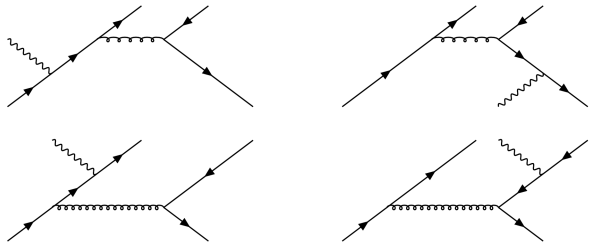


FIG. 1: One-hard-gluon-exchange Feynman diagrams for the parton-level subprocess $\gamma q \rightarrow Mq$ in the single meson photoproduction $\gamma N \rightarrow MN$.

the parton-level subprocess amplitude for pseudoscalar meson photoproduction. Due to isospin invariance, the form factors are divided out and the exclusive charged pion ratio takes on a simple form,

$$\frac{d\sigma/dt(\gamma n \rightarrow \pi^- p)}{d\sigma/dt(\gamma p \rightarrow \pi^+ n)} \simeq \left(\frac{ue_d + se_u}{ue_u + se_d} \right)^2, \quad (4)$$

where u and s are the Mandelstam variables and e_q denotes the charge of quark q .

III. EXPERIMENT

To study the transition from nucleon-meson degrees of freedom to quark-gluon degrees of freedom, it is essential to investigate the GeV region where the transition appears to occur. While there were some measurements at SLAC for the $\gamma p \rightarrow \pi^+ n$ process at photon energies of 4, 5 and 7.5 GeV [9], which exhibit a global scaling behavior expected by the constituent counting rule, there are no data beyond 2 GeV for $\gamma n \rightarrow \pi^- p$ [44]. This experiment, JLab experiment E94-104 [18] was proposed to measure the cross section for charged pion photoproduction $d\sigma/dt(\gamma n \rightarrow \pi^- p)$ and $d\sigma/dt(\gamma p \rightarrow \pi^+ n)$ from 1.1 to 5.5 GeV. In addition, the differential cross section ratio for charged pion photoproduction can be formed and compared to theoretical predictions.

JLab experiment E94-104 was carried out in Hall A, using the continuous electron beam at currents around 30 μA . The basic instrumentation for JLab Hall A was described in reference [45]. The schematic view of the setup for this experiment is shown in Figure 2. Real bremsstrahlung photons were generated by the electrons impinging on a copper radiator. A liquid hydrogen target was used as the proton target, while a liquid deuterium target was used as an effective neutron target. The outgoing pions and protons were detected by the two high resolution spectrometers (HRS) in Hall A. Based on two-body kinematics, the incident photon energies were reconstructed from the final states, i.e. the momentum and angle of the π^+ in the singles measurements for the $\gamma p \rightarrow \pi^+ n$ process, or momenta and angles of the π^- and p in the coincidence measurements for the $\gamma n \rightarrow \pi^- p$

process.

The coincidence kinematics for the $\gamma n \rightarrow \pi^- p$ process are listed in Table I. Normally, the negatively charged pions are detected by the spectrometer to the right of the beam line (viewed along the beam direction), and the protons detected by the left spectrometer. But a few kinematics require reversing the polarities of the spectrometers, because the maximum momentum of the right spectrometer is only 3.16 GeV/c, while that of the left spectrometer is 4 GeV/c. The singles kinematics for the $\gamma p \rightarrow \pi^+ n$ process are listed in Table II. The positively charged pions were detected by the left spectrometer with positive polarity. The beam energies tabulated in Table I and Table II were the nominal values used to set the spectrometers, which may deviate from the measured ones by several MeV. The spectrometer momentum and angle settings were calculated by using a photon energy close to the beam energy, i.e. $E_e - 75$ (MeV), where the multiple pion production processes were suppressed.

The electron accelerator at JLab [46] is the first large-scale application of superconducting radio-frequency electron accelerating technology. It can deliver a high-quality continuous polarized ($>75\%$) electron beam with current up to 200 μA and energy up to 5.7 GeV to three halls. The energy of the electron beam delivered to Hall A can be determined absolutely to the precision of 0.02% [45]. The real bremsstrahlung photon beam is generated by electrons impinging on a copper radiator, located 72.6 cm upstream from the target. The foil with a thickness of 6.12% radiation length was used for the production data of E94-104.

The basic cryogenic target consisted of three independent loops: a liquid hydrogen (LH2) loop at a temperature of 19 K, a liquid deuterium (LD2) loop at 22 K and a gaseous helium loop at 5.8 K. Each of the liquid loops, LH2 and LD2, contained two horizontal aluminum cylindrical target cells, 15 cm and 4 cm along the beam direction and 63.5 mm (2.5 in) in diameter. Besides the cryogenic target cells, there were also some solid targets on the target lifter: a BeO target for beam spot display, single foil and 9-foil carbon targets for optics optimization, and 4 cm, 10 cm and 15 cm dummy targets with two thin pieces of aluminum pieces for measuring the contributions from target windows. The density of the cryogenic target was determined from the temperature and the pressure, which is 0.0723 g/cm³ for LH2 target and 0.167 g/cm³ for LD2 target.

The core of the Hall A equipment [45] is a pair of nearly identical 4 GeV/c spectrometers capable of determining the momentum and angles of charged particles with high resolution. The detector packages for experiment E94-104 are shown in Figure 2. When a particle goes through either spectrometer, the vertical drift chambers (VDCs) recorded its track, which can be used to reconstruct its momentum, scattering angle and reaction vertex at the target. The scintillator planes (S1/S2) provided timing information and generated triggers. The left spectrometer was optimized to detect positively charged

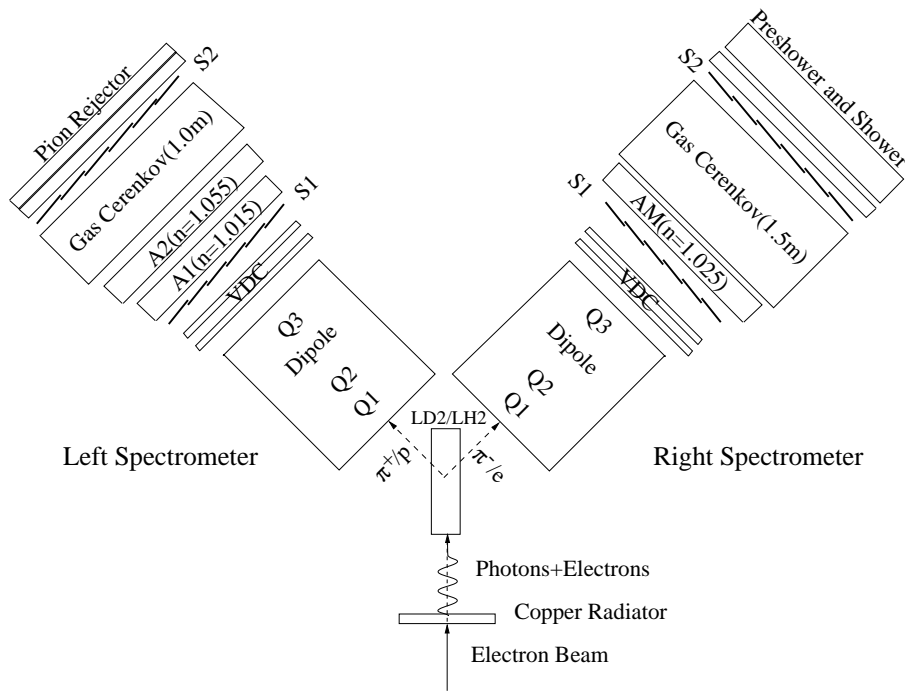


FIG. 2: Schematic view of the experimental setup for E94-104.

TABLE I: Spectrometer settings for coincidence kinematics. E_e is the electron beam energy, $\theta_{c.m.}$ the pion center-of-mass angle, P_L (P_R) the central momentum for left (right) spectrometer with the sign indicating its polarity, and θ_L (θ_R) is the central scattering angle for left (right) spectrometer. The Mandelstam variables \sqrt{s} and $-t$ are in the last two columns.

E_e (GeV)	$\theta_{c.m.}$ ($^\circ$)	P_L (GeV/c)	θ_L ($^\circ$)	P_R (GeV/c)	θ_R ($^\circ$)	\sqrt{s} (GeV)	$-t$ (GeV/c) 2
1.173	50.0	+0.521	60.17	-0.953	28.33	1.71	0.253
1.173	70.0	+0.727	49.72	-0.838	41.45	1.71	0.467
1.173	90.0	+0.923	39.75	-0.706	56.66	1.71	0.709
1.721	50.0	+0.697	58.32	-1.433	24.46	1.99	0.433
1.721	70.0	+0.989	47.39	-1.238	36.02	1.99	0.798
1.721	90.0	+1.277	37.37	-1.015	49.73	1.99	1.212
1.875	50.0	+0.742	57.79	-1.566	23.64	2.06	0.484
1.875	90.0	+1.370	36.75	-1.099	48.21	2.06	1.355
2.558	50.0	+0.913	55.67	-2.108	20.96	2.35	0.696
2.558	70.0	+1.322	44.37	-1.794	31.02	2.35	1.282
2.558	90.0	+1.740	34.45	-1.438	43.18	2.35	1.948
2.558	50.0	-2.108	20.96	+0.913	55.67	2.35	0.696
2.558	70.0	-1.794	31.02	+1.322	44.37	2.35	1.282
2.558	90.0	-1.438	43.18	+1.740	34.45	2.35	1.948
3.395	50.0	+1.113	53.21	-2.799	18.57	2.67	0.971
3.395	70.0	+1.642	41.74	-2.363	27.56	2.67	1.789
3.395	90.0	+2.195	32.01	-1.866	38.57	2.67	2.718
3.395	100.0	+2.466	27.69	-1.614	45.24	2.67	3.190
3.395	110.0	+2.725	23.65	-1.369	53.01	2.67	3.648
4.232	50.0	-3.489	16.84	+1.300	51.04	2.95	1.248
4.232	70.0	+1.949	39.51	-2.929	25.05	2.95	2.299
4.232	90.0	+2.638	30.01	-2.291	35.18	2.95	3.494
5.618	70.0	-3.863	22.08	+2.442	36.48	3.36	3.148
5.618	90.0	+3.359	27.38	-2.990	31.11	3.36	4.785

TABLE II: Spectrometer settings for singles kinematics. E_e is the electron beam energy, $\theta_{c.m.}$ the pion center-of-mass angle, P_L the central momentum for left spectrometer with the sign indicating its polarity, and θ_L is the central scattering angle for left spectrometer. The Mandelstam variables \sqrt{s} and $-t$ are in the last two columns.

E_e (GeV)	$\theta_{c.m.}$ ($^\circ$)	P_L (GeV/c)	θ_L ($^\circ$)	\sqrt{s} (GeV)	$-t$ (GeV/c) ²
1.173	70.0	+0.838	41.45	1.71	0.467
1.173	90.0	+0.706	56.66	1.71	0.709
1.721	50.0	+1.433	24.46	1.99	0.433
1.721	70.0	+1.238	36.02	1.99	0.798
1.721	90.0	+1.015	49.73	1.99	1.212
1.875	50.0	+1.566	23.64	2.06	0.484
1.875	90.0	+1.099	48.21	2.06	1.355
2.558	50.0	+2.108	20.96	2.35	0.696
2.558	70.0	+1.794	31.02	2.35	1.282
2.558	90.0	+1.438	43.18	2.35	1.948
3.395	50.0	+2.799	18.57	2.67	0.971
3.395	70.0	+2.363	27.56	2.67	1.789
3.395	90.0	+1.866	38.57	2.67	2.718
3.395	100.0	+1.614	45.24	2.67	3.190
3.395	110.0	+1.369	53.01	2.67	3.648
4.232	70.0	+2.929	25.05	2.95	2.299
4.232	90.0	+2.291	35.18	2.95	3.494
4.232	100.0	+1.967	41.36	2.95	4.101
5.618	90.0	+2.990	31.11	3.36	4.785
5.618	100.0	+2.547	36.69	3.36	5.615

particles while the right one was optimized to detect negatively charged particles. However, both spectrometers had to contain detectors to identify negatively and positively charged particles, since there were a few reversed polarity kinematics. Aerogel Čerenkov detectors (A1/A2/AM) provided particle identification for positively charged particles, mainly pions and protons. Gas Čerenkov, preshower/shower detector and pion rejector were used to discriminate negatively charged particles, mainly electrons and pions. Different types of particles can be easily identified, as shown in Figure 3.

IV. DATA ANALYSIS

A. Overview

The raw data from the data acquisition (DAQ) system were replayed or decoded by an event processing program, ESPACE (Event Scanning Program for Hall A Collaboration Experiments) using CERNLIB packages. The outputs were histograms and ntuples of physical variables in the HBOOK format. The yield from the data was obtained by applying cuts on certain variables in the ntuples, such as trigger type, particle type, spectrometer acceptance and reconstructed photon energy. Next, the yield was normalized by beam charge and computer deadtime. To extract the differential cross sections, simulations were carried out by using the modified MCEEP (Monte Carlo for ($e, e'p$)) program [47] written for JLab

Hall A. The raw differential cross section $(\frac{d\sigma}{dt})_{\text{data}}$ was extracted by comparing the background subtracted yield from the data (Y_{data}) with the yield from the Monte Carlo simulation (Y_{mc}):

$$\left(\frac{d\sigma}{dt}\right)_{\text{data}} = \left(\frac{d\sigma}{dt}\right)_{\text{mc}} * \frac{Y_{\text{data}}}{Y_{\text{mc}}}. \quad (5)$$

Finally to extract the physical differential cross section, corrections such as the nuclear transparency of deuterium for the final state interaction, the detection efficiency and nuclear absorption in the detection materials were applied to the raw differential cross section.

B. Acceptance Analysis

The R-function is defined to be the minimal distance to the acceptance boundary in terms of several two-dimensional polygons. It helps to select events in the central region of the spectrometer acceptance in a systematic and efficient way, where the optics matrix elements are well tuned. This method was originally developed in the E89-044 data analysis [51]. The version [52] refined in the E91-011 data analysis was used to analyze the E94-104 data and will be discussed below.

The R-function is generated for each event in both data analysis and simulation to optimize the cuts on different acceptance variables, i.e. θ_{tg} , ϕ_{tg} , y_{tg} and δ . The θ_{tg} is the deviation of the out-of-plane angle from the spectrometer central setting of zero. The ϕ_{tg} is the deviation

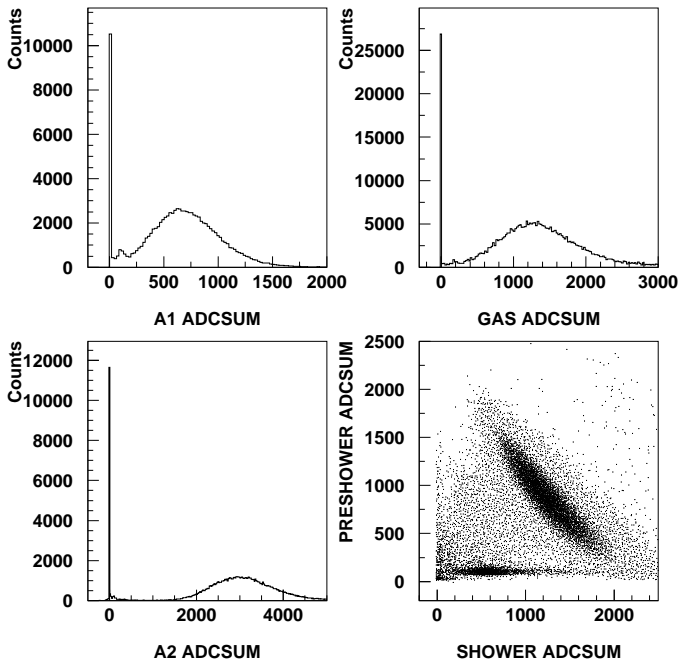


FIG. 3: Performance of particle identification detectors with normal polarities of the spectrometers (at central momenta of 1.8 GeV). The 'ADCSUM' is the sum of the calibrated ADC spectra from the PMTs to detect Čerenkov photons. With the pedestal at 0, the single photoelectron peak of A1/A2 and gas Čerenkov detector was calibrated to be at channel 100 and at channel 150 respectively. Pions should generate some photoelectrons when passing A1/A2 while protons should not. Electrons should generate some photoelectrons when passing gas Čerenkov detector while pions should not. The sum of preshower and shower ADC for the electrons was equal to the total energy.

of the in-plane angle from the central setting of scattering angle. The y_{tg} is the reaction vertex position in the target along the direction perpendicular to the spectrometers. The δ is the relative deviation from the central momentum setting.

Six two-dimensional boundaries are defined for each spectrometer, out of any two combinations of the four acceptance variables, θ_{tg} , ϕ_{tg} , y_{tg} and δ . Each boundary is a polygon defined in a two-dimension plot of the data. For each event, the magnitude of the distance to the boundary is normalized based on the maximal length. The sign of the distance is positive for the events inside the polygon. The R-function for a single spectrometer, useful for singles $\gamma p \rightarrow \pi^+ n$ data, is defined to be the minimal distance to the six boundaries, while that for two spectrometers, useful for coincidence $\gamma n \rightarrow \pi^- p$ data, is defined by twelve two-dimension boundaries.

C. Particle Identification Analysis

For the detection of positively charged particles, the protons need to be selected for the coincidence $\gamma n \rightarrow \pi^- p$ process and the pions need to be selected for the singles $\gamma p \rightarrow \pi^+ n$ process. The aerogel Čerenkov detectors A1/A2/AM (see Figure 2) were utilized to identify protons and pions. The A1 and A2 detectors were used for normal polarity data, while AM was used for reversed polarity data. The particle identification with aerogel detectors was consistent with other methods available at low momentum, for example measuring the Time-Of-Flight of the particle or the energy deposited in the scintillators.

For the detection of negatively charged particles, the pions need to be identified from the electron background for the coincidence $\gamma n \rightarrow \pi^- p$ process. It was realized by using the combination of the gas Čerenkov and shower-type detector, i.e. the gas Čerenkov and total shower (preshower/shower) detector for normal polarity kinematics, the gas Čerenkov and pion rejector detector for reversed polarity kinematics. A one-dimensional cut was used for gas Čerenkov detector, while a two-dimensional graphic cut was defined for the shower-type detector.

D. Background Subtraction

The production data contained various kinds of background, such as those from the electroproduction process and those from the end caps of the target. Therefore each complete kinematics consisted of four different configurations for data taking,

- (1) Radiator in, production target,
- (2) Radiator in, background target,
- (3) Radiator out, production target,
- (4) Radiator out, background target.

For the coincidence $\gamma n \rightarrow \pi^- p$ process, the LD2 target was used as the production target and the LH2 target for the background subtraction. For the singles $\gamma p \rightarrow \pi^+ n$ process, the LH2 target was used as the production target and the dummy target for the background subtraction.

The backgrounds were subtracted from the coincidence π^- or singles π^+ production yield according to

$$\begin{aligned} \pi^- &: (Y_{in,LD2} - Y_{in,LH2}) - f(E_\gamma)(Y_{out,LD2} - Y_{out,LH2}) \\ \pi^+ &: (Y_{in,LH2} - Y_{in,Dum}) - f(E_\gamma)(Y_{out,LH2} - Y_{out,Dum}) \end{aligned} \quad (6)$$

where the in or out represents using or removing the radiator during the data taking. The factor $f(E_\gamma)$ is less than unity due to the interaction between the radiator and the electron beam. For most kinematics, the yield without the radiator was about one third of that with the radiator. The yield without the production target, especially for coincidence cases, was much smaller than the production yield.

E. Monte Carlo Simulation

The Monte Carlo simulation was performed by using MCEEP [47], a computer program designed for coincidence ($e, e'X$) experiments in Hall A. The MCEEP program employs a uniform random sampling method to populate the experimental acceptance. An event is defined as one combination of variables that completely specifies the reaction in the laboratory. The cross section is considered as the weight of the event. It was modified for the coincidence $n(\gamma, \pi^- p)$ and singles $p(\gamma, \pi^+)n$ processes. The program was also modified to generate the R-function to define the acceptance cuts.

The momentum distribution of the neutron inside the deuterium target was considered in calculating the kinematics and cross section. The bremsstrahlung photon energy was randomly generated and the bremsstrahlung photon yield spectrum was calculated using thin-radiator calculation based on reference [48], which was later corrected by the thick-radiator calculation. The pion survival factor was also included in the cross section calculation based on the average flight length and was later corrected by muon contamination.

The differential cross section $\frac{d\sigma}{dt}$ for π^+ photoproduction at fixed center-of-mass angle was assumed to be

$$\frac{d\sigma}{dt} = \frac{0.69 F_{\text{survive}}}{(1 + \cos\theta_{c.m.})^4 (1 - \cos\theta_{c.m.})^5} \cdot \left(\frac{s_0}{s}\right)^7, \quad (7)$$

where the angular distribution was fitted to SLAC data in the several GeV region [9]. The factor of 0.69 and $s_0 = 10.263$ came from these SLAC data at 5 GeV. The s^{-7} dependence was consistent with the constituent counting rule. For π^- photoproduction, there was another constant to account for the deviation from π^+ photoproduction, but the overall normalization factor did not affect the final cross section extraction. The pion survival factor F_{survive} was calculated by $F_{\text{survive}} = \exp\left(-\frac{L}{\gamma_\pi \tau_\pi \beta_\pi c}\right)$, with the average flight length L of 25 m and pion mean lifetime of $\tau_\pi = 2.60 \times 10^{-8}$ s.

The distributions of different variables from the data were compared with those from the Monte Carlo simulation, including the acceptance variables, the reconstructed photon energy, the reconstructed initial momentum distribution of neutron inside the deuterium target, and the reconstructed center-of-mass angle, as shown in Figure 4 to Figure 10. The results from data are symbolized by solid circles for coincidence measurements or by solid squares for singles measurements, while those from simulation are plotted as lines. Each simulated spectrum was multiplied by an arbitrary normalization factor for the comparison. This normalization factor is directly related to the cross section extraction, as shown in Equation 5. Except for the photon energy comparisons, only one typical kinematic setting is shown for other cases, i.e. the one at $E_e = 4236$ MeV and $\theta_{c.m.} = 90^\circ$ for the coincidence measurements, or at $E_e = 4236$ MeV and $\theta_{c.m.} = 90^\circ$ for the singles measurements.

The overall agreement between data and simulation is good, but there is some discrepancy for some cases. Since only reaction of interest was considered in the simulation, some discrepancy may be due to other physical reactions such as the multi-pion production. But the contribution from the multi-pion production is negligible with the cut on photon energy, as shown by the shaded area in Figure 6 and Figure 7. The uncertainties associated with various measurements such as the acceptance will affect the agreement too, which was included into the systematic uncertainties.

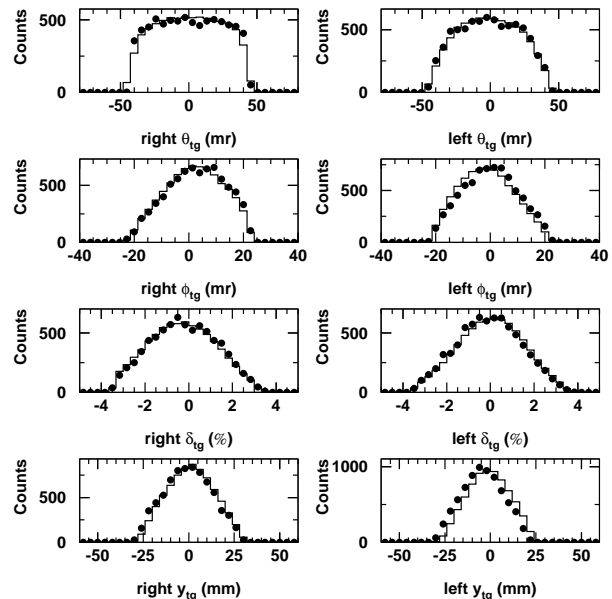


FIG. 4: Comparison of acceptance variables from left and right spectrometers between data and simulation for coincidence measurements.

F. Corrections and Uncertainties

Table III lists the systematic uncertainties for kinematics at $\theta_{c.m.} = 90^\circ$. The kinematics at other angles have similar breakdowns.

The thin-radiator calculation embedded in the simulation to calculate the photon flux was corrected for the radiator thickness, by using a thick-radiator code [49] based on references [48, 50], which considers the energy loss of electrons in the radiator and is expected to be accurate to a level of 3% for the energies and radiator thickness used in this experiment. For the 6.12% copper radiator, the thin-radiator calculation overestimates the yield by 11% to 20%. By using this code [49], the $f(E_\gamma)$ can be also calculated, which will affect the subtraction of electron induced background.

The decrease of target density due to beam induced local boiling was corrected. According to a comparison of the normalized yields with different beam currents, this correction was proportional to the average beam current

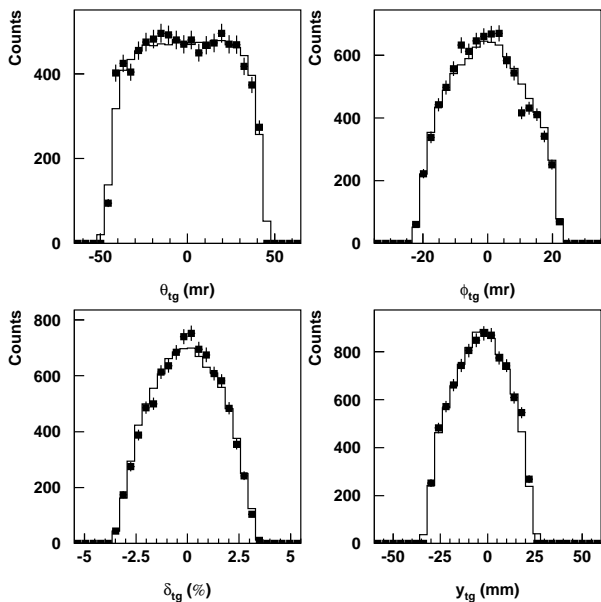


FIG. 5: Comparison of acceptance variables from left spectrometers between data and simulation for singles measurements.

TABLE III: The systematic uncertainties for coincidence and singles measurements at $\theta_{c.m.} = 90^\circ$.

Kinematics	Coincidence (%)	Singles (%)
Photon Yield	3.0	3.0
$f(E_\gamma)$	1.0	1.0
Target Density	1.0	1.0
Tracking	3.0	2.0
Scintillator/Trigger	1.3	1.0
PID	2.2	3.0
Muon Contamination	3.0	3.0
Transparency	5.0	-
Nuclear Absorption	4.2	3.0
Trial Cross Section	2.2	2.2
Deadtime	2.0	2.0
Acceptance	3.0	3.0
Energy Loss	2.0	2.0
Random Coincidence	1.0	-
Momentum Distribution	1.0	-
Beam Charge	1.0	1.0
Total	10.1	8.1

and can be parameterized as $0.072 * I$ (%) for LD2 target and $0.048 * I$ (%) for the LH2 target with I the beam current in the unit of μA . The uncertainty was on the level of 1%.

The single wire efficiency of the VDCs, with samples defined by two neighboring wires, was very close to 100%. But multi-track events, dominated by two-track events, may still cause inefficiency in tracking. The corrections were applied based on the ratios of multi-track to single-

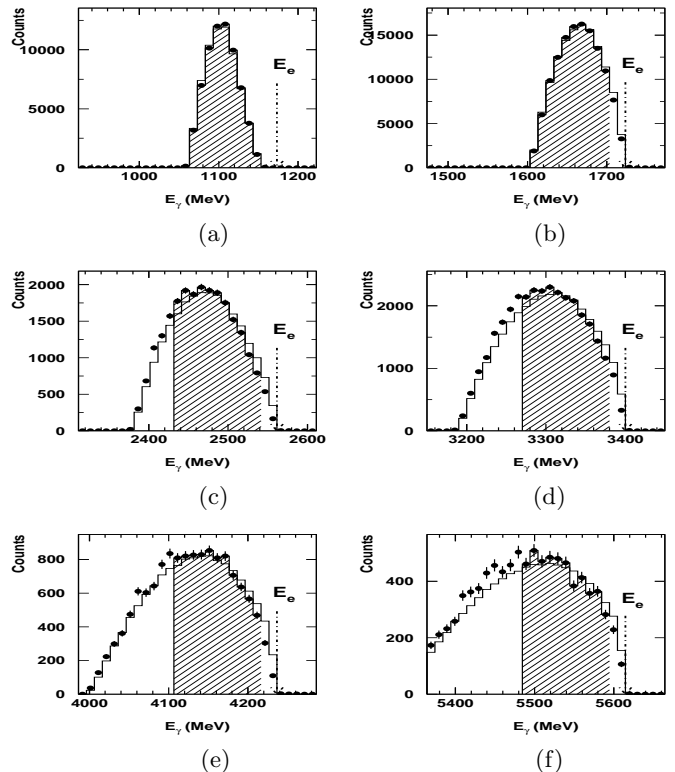


FIG. 6: Comparison of reconstructed photon energy between data and simulation for coincidence measurements at $\theta_{c.m.} = 90^\circ$. The results from data are plotted as symbols, while those from simulation are plotted as lines. The electron beam energies are 1173.3, 1723.4, 2561.5, 3400.0, 4236.4 and 5614.4 MeV. The comparison at beam energy 1876.9 MeV (not shown here) is very similar to that at 1723.4 MeV. The shaded events were chosen to extract the differential cross section.

track events, which were less than 2% for most kinematics. The additional inefficiency associated with the track reconstruction algorithm was included in the uncertainty of 3%.

The scintillator/trigger efficiency was obtained by checking the trigger for those selected events with good signals in VDCs and PID detectors. Special data were taken to measure the efficiency, which was averaged to be $98.8 \pm 1.1\%$ for the right spectrometer and $98.8 \pm 0.7\%$ for the left spectrometer.

One need to identify protons and negative pions for coincidence π^- photoproduction, and identify only positively charged pions for singles π^+ photoproduction. There is no correction on proton identification for coincidence π^- photoproduction due to the very high p/π^+ ratio (> 100). The uncertainty due to δ -electrons (or knock-on electrons) was estimated to be 1%. For pion selection from coincidence π^- photoproduction and singles π^+ photoproduction, two PID detectors were used. The correction and uncertainty were estimated based on the performance study of each detector by defining good

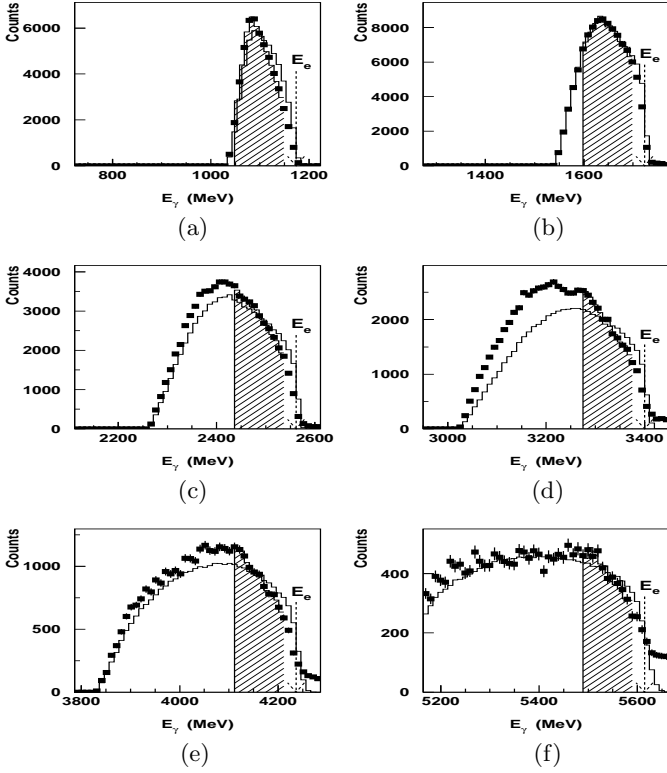


FIG. 7: Comparison of reconstructed photon energy between data and simulation for singles measurements at $\theta_{c.m.} = 90^\circ$. The results from data are plotted as symbols, while those from simulation are plotted as lines. The electron beam energies are 1173.3, 1723.4, 2561.5, 3400.0, 4236.4 and 5614.4 MeV. The comparison at beam energy 1876.9 MeV (not shown here) is very similar to that at 1723.4 MeV. The shaded events were chosen to extract the differential cross section.

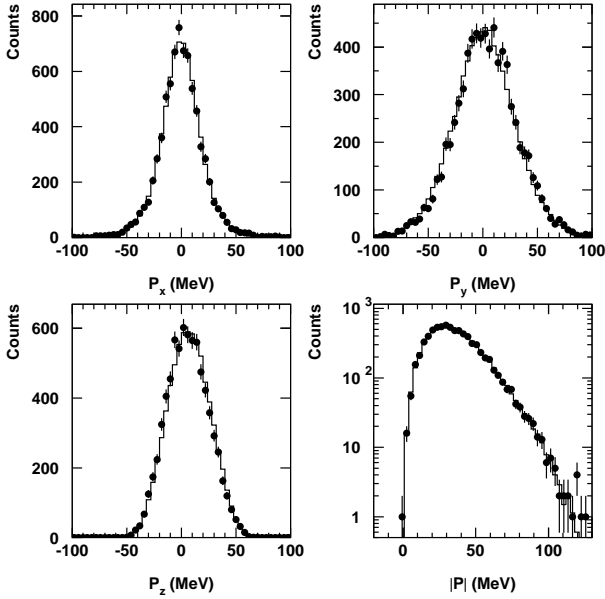


FIG. 8: Comparison of reconstructed momentum distribution of the neutron in the deuteron target between data and simulation for coincidence measurements.

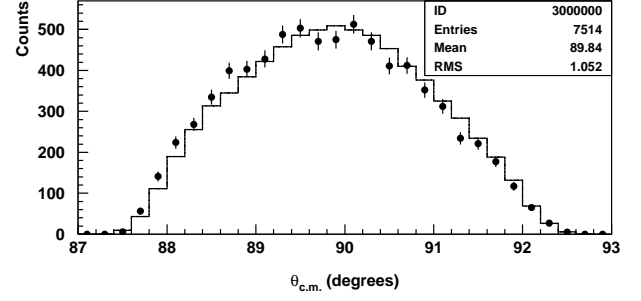


FIG. 9: Comparison of reconstructed center-of-mass angle between data and simulation for coincidence measurements. The nominal center-of-mass angle is 90 degrees.

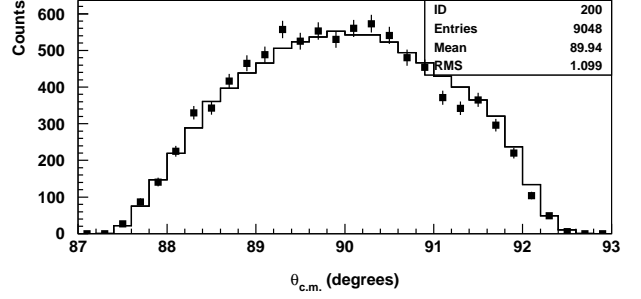


FIG. 10: Comparison of reconstructed center-of-mass angle between data and simulation for singles measurements. The nominal center-of-mass angle is 90 degrees.

event samples based on the other one. The corrections depended on the particle momentum and the signal to noise ratio, and therefore varied by kinematics.

The pion decay loss was considered as the survival factor in the simulation by using the pion flight length and pion lifetime. The survival factor ranges from 53% to 89% for different pion momentum. However, since some of the muons from pion decay may still fall into the acceptance and be misidentified as pions, the calculation above may underestimate the effective pion survival factor and should be corrected. Based on the estimation with the modified simulation program SIMC, the correction depended on the particle momentum and ranged from -7% to -4% approximately [54]. The uncertainty was estimated to be 3% by checking the dependence of the correction on the acceptance cuts.

Nuclear effects must be considered to obtain the cross section for $\gamma n \rightarrow \pi^- p$ from the measurement of $d(\gamma, \pi^- p)p$. The cross section may be reduced due to the final state interactions with the spectator proton inside the deuteron. The nuclear transparency was defined to be the ratio of the reduced cross section to the raw cross section without any final state interactions. The measured nuclear transparencies for $d(e, e'p)$ quasi-elastic scattering [55], show little Q^2 dependence above $Q^2 \simeq 2$ (GeV/c^2) and agree well with a Glauber calculation [56].

The fitted value of 0.904 ± 0.013 was used to deduce the nuclear transparency for the experiment E94-104, based on the Glauber formulation. The nuclear transparency for $d(\gamma, \pi^- p)p$ was scaled from that of $d(e, e'p)n$ by replacing the total pn scattering cross section with the total pp and $\pi^- p$ scattering cross sections. The systematic uncertainties in the nuclear transparency were estimated to be 5% to account for the uncertainties in the nuclear transparency measurement for $d(e, e'p)n$ and those in the effective pn , pp and $\pi^- p$ scattering cross sections.

The produced particles, pions and protons in the coincidence measurements and pions in the singles measurements, had to go through various materials in the target and spectrometers before being detected. The event loss in the material is called nuclear absorption here. The major sources of nuclear absorption for high energy protons are listed in Table IV. The absorption was calculated based on the thickness and effective absorption length of the material in the flight path of the produced particles. The effective absorption length $\bar{\lambda}$ was estimated from the nuclear collision length λ_T and nuclear interaction length λ_I [57] as $2\lambda_T\lambda_I/(\lambda_T + \lambda_I)$ by assuming that half of the elastic and quasi-elastic scattering contribute to the absorption. Later, the nuclear absorption was adjusted due to different flight lengths in the target, and different effective absorption lengths for pions and protons at various momenta. The flight length can be calculated from the scattering angle and the geometry of the target. The energy dependence of the effective absorption length was obtained from the cross section data in Reference [57]. The uncertainty for each produced hadron was estimated to be 3%.

TABLE IV: Major nuclear absorption in the target and spectrometer for high energy protons.

Material	Thickness (cm)	Density (g/cm ³)	λ (g/cm ²)	Absorp. (%)
15cm LD2 (19K)	5.5	0.1670	49.8	1.84
15cm LH2 (22K)	5.5	0.0723	46.8	0.85
air	300.	1.21e-3	73.4	0.49
S1 (Polystyrene)	0.5	1.032	68.3	0.76
S2 (Polystyrene)	0.5	1.032	68.3	0.76
A1 (Aerogel)	9.0	0.060	75.5	0.72
A2 (Aerogel)	5.0	0.220	75.5	1.46
AM (Aerogel)	9.0	0.100	75.5	1.19
Gas Čerenkov (CO ₂)	150.	1.98e-3	73.6	0.40

The final cross section, extracted by comparing data and simulation, depended on the angular distribution and energy dependence of the trial cross section as the input of the simulation. Instead of searching for the exact form of the angular distribution and energy dependence of the actual cross section, the cross section fitted to SLAC data at high energy [9] was used and its deviation from the actual cross section was considered as the systematic uncertainty. The trial angular distribution in the simulation

may not be the same as the real case. The resulting systematic uncertainty was estimated by checking the change of the final cross section from the flat angular distribution. The changes of the final results were very small due to the small acceptance of the Hall A spectrometers. In the comparison, the mean center-of-mass angles were determined from the data, which deviated from those determined from the simulation by 0.2° at most. The systematic uncertainties due to the angular distribution were estimated to be 1%, 2% and 3% for kinematics at $\theta_{c.m.} = 90^\circ, 100^\circ$, at $\theta_{c.m.} = 70^\circ, 110^\circ$, and at $\theta_{c.m.} = 50^\circ$ respectively. The trial cross section used in the simulation had a s^{-7} energy dependence, which was suggested by the SLAC data at high energy [9] and was predicted by the constituent counting rule. The actual energy dependences for both coincidence and singles kinematics are shown in Section V. The data, especially at low energy, do not have the s^{-7} energy dependence. The resulting systematic uncertainty was assigned to be 2%, by checking the change of the final cross section from the flat energy dependence.

The computer deadtime was calculated as the ratio of missed triggers in the data stream from DAQ to the input triggers from scalers. It was less than 20% for nearly all the data and was corrected run-by-run (not listed here). The uncertainty was estimated to be around 10% of the correction. The electronics deadtime was less than 0.5% for the majority of E94-104 data based on measurements using test pulses. There were also other systematics uncertainties for example due to acceptance, energy loss, random coincidence subtraction and beam charge.

G. Reversed Polarity Data

The polarities of the spectrometers were reversed for a few kinematics during the experiment. The particle identification was optimized for data acquisition with normal polarities. The aerogel detector (AM) in the right spectrometer was not as good as the combination of two aerogel detectors (A1 and A2) in the left spectrometer in identifying protons. But since the proton signals are very clean with very low pion background, this hardly affected the results. The gas Čerenkov detector and pion rejector in the left spectrometer did not perform as well as the gas Čerenkov detector and preshower/shower detector in the right spectrometer in identifying pions. A tighter cut on momentum ($-4\% < \delta < 0\%$) was applied in the data analysis to avoid using the bad PMTs in the left gas Čerenkov detector. The pion rejector was only used to estimate the corrections. The reconstructed photon energy spectrum from the data agreed with that from the simulation, as shown in Figure 11. For a consistency check, there were also some data recorded with both normal polarities and reversed polarities. The differences in yields were within 5%, smaller than the systematic uncertainties (on the level of 10%).

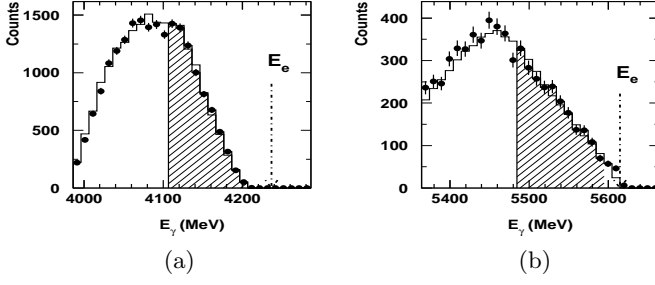


FIG. 11: Comparison of reconstructed photon energy between data and simulation for coincidence π^- photoproduction with reversed polarities. The plot on the left represents the kinematics at $E_e = 4236.4$ MeV and $\theta_{c.m.} = 50^\circ$, while the plot on the right represents the kinematics at $E_e = 5614.4$ MeV and $\theta_{c.m.} = 70^\circ$.

V. RESULTS AND DISCUSSION

The differential cross sections $d\sigma/d\Omega$ and $s^7 d\sigma/dt$ extracted from JLab experiment E94-104 are shown in Table V and Table VI for different beam energies and pion center-of-mass angles. The published results at 90° [19] are also updated here. The angular distributions for all the energies are plotted in Figure 12 and Figure 13. Also plotted are the SLAC π^+ data at $E_\gamma = 4, 5, 7.5$ GeV [9]. Both the π^+ and π^- data at comparable energies, i.e. $E_\gamma = 4.2, 5.5$ GeV, are consistent with the fit of the high energy SLAC data.

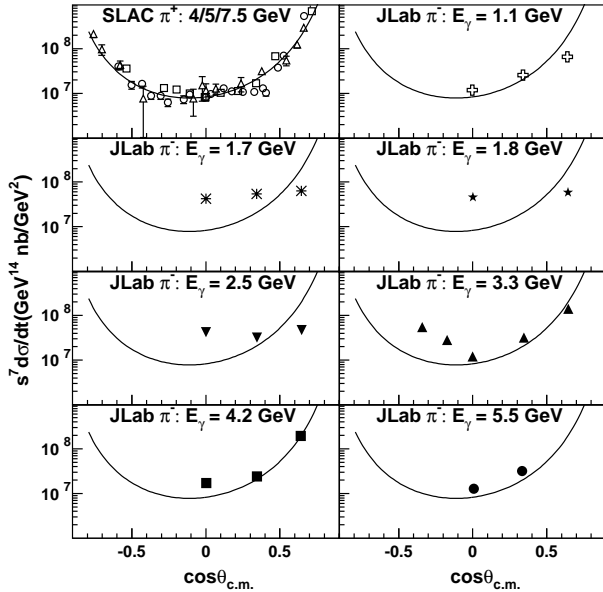


FIG. 12: Angular distributions from JLab E94-104 for the $\gamma p \rightarrow \pi^+ n$ process, as well as those from the SLAC data [9] for the $\gamma p \rightarrow \pi^+ n$ process at photon energy of 4 GeV (open squares), 5 GeV (open circles), and 7.5 GeV (open triangles). The curve in each panel is the empirical fit of SLAC data: $0.828e7 \cdot (1 - \cos\theta_{c.m.})^{-5} \cdot (1 + \cos\theta_{c.m.})^{-4}$.

+

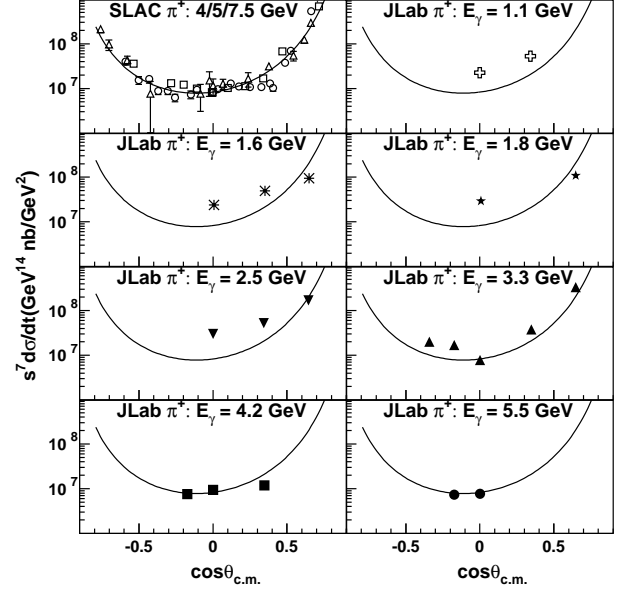


FIG. 13: Angular distributions from JLab E94-104 for the $\gamma p \rightarrow \pi^+ n$ process, as well as those from the SLAC data [9] for the $\gamma p \rightarrow \pi^+ n$ process at photon energy of 4 GeV (open squares), 5 GeV (open circles), and 7.5 GeV (open triangles). The curve in each panel is the empirical fit of SLAC data: $0.828e7 \cdot (1 - \cos\theta_{c.m.})^{-5} \cdot (1 + \cos\theta_{c.m.})^{-4}$.

It is worth mentioning that the pQCD calculations involving gluon self-coupling [60] cannot reproduce the angular distribution of the SLAC data, especially at the backward angles. This discrepancy may be due to the relatively low values of s , $|t|$ and u . The main contamination of their leading-twist predictions came from the t -channel meson resonances at forward angles, and from the u -channel baryon resonances at backward angles.

A. Comparison with the World Data

As shown in Figure 14 and Figure 15, the data from JLab experiment E94-104 (in solid circles) extended the single pion photoproduction measurements at several GeV [9, 44, 58, 59], by spanning the resonance region and the scaling region. The differential cross sections of the $\gamma n \rightarrow \pi^- p$ process with \sqrt{s} greater than 2.2 GeV were measured for the first time. The uncertainty in \sqrt{s} due to the 100 MeV photon energy window ranges from 0.05 to 0.03 GeV as the beam energy increases

The data agree within uncertainties with the world data in the overlapping energy region, except with the Besch *et al.* data [58] (open triangles). The Besch *et al.* data from Bonn suggest a very sharp peak in the scaled cross section for the $\gamma n \rightarrow \pi^- p$ process with \sqrt{s} around 2.0 GeV. Our data confirm the scaled cross section enhancement around that region, but the peak is much less pronounced. We do not know the origin of this discrepancy exactly, though our momentum resolution (0.02%) is much better than that of Besch *et al.* (4%). The broad

TABLE V: Differential cross sections for the $\gamma n \rightarrow \pi^- p$ process followed by the statistical and systematic uncertainties.

E_e (GeV)	E_γ (GeV)	\sqrt{s} (GeV)	$\theta_{c.m.}$ ($^\circ$)	$(\frac{d\sigma}{d\Omega})_{c.m.}$ ($\mu\text{b}/\text{sr}$)	$s^T \frac{d\sigma}{dt}$ ($10^7 \text{ nb} \cdot \text{GeV}^{12}$)
5.614	5.536	3.36	89.6	$(4.22 \pm 0.09 \pm 0.42) \times 10^{-4}$	$1.28 \pm 0.03 \pm 0.13$
	5.529	3.36	70.5	$(1.05 \pm 0.03 \pm 0.12) \times 10^{-3}$	$3.17 \pm 0.08 \pm 0.35$
4.236	4.158	2.95	89.8	$(2.56 \pm 0.04 \pm 0.26) \times 10^{-3}$	$1.71 \pm 0.03 \pm 0.17$
	4.157	2.95	69.8	$(3.64 \pm 0.07 \pm 0.40) \times 10^{-3}$	$2.43 \pm 0.05 \pm 0.27$
	4.141	2.94	50.1	$(2.95 \pm 0.07 \pm 0.32) \times 10^{-2}$	$19.3 \pm 0.45 \pm 2.13$
3.400	3.321	2.67	90.1	$(5.66 \pm 0.06 \pm 0.57) \times 10^{-3}$	$1.20 \pm 0.01 \pm 0.12$
	3.321	2.67	69.8	$(1.50 \pm 0.02 \pm 0.16) \times 10^{-2}$	$3.19 \pm 0.03 \pm 0.35$
	3.322	2.67	49.8	$(6.63 \pm 0.09 \pm 0.73) \times 10^{-2}$	$14.1 \pm 0.20 \pm 1.55$
	3.320	2.67	100.0	$(1.34 \pm 0.03 \pm 0.13) \times 10^{-2}$	$2.85 \pm 0.06 \pm 0.28$
	3.322	2.67	110.0	$(2.60 \pm 0.04 \pm 0.26) \times 10^{-2}$	$5.53 \pm 0.09 \pm 0.55$
2.561	2.481	2.36	89.9	$(8.24 \pm 0.10 \pm 0.82) \times 10^{-2}$	$4.24 \pm 0.05 \pm 0.42$
	2.482	2.36	69.8	$(6.18 \pm 0.08 \pm 0.68) \times 10^{-2}$	$3.19 \pm 0.04 \pm 0.35$
	2.484	2.36	49.7	$(9.06 \pm 0.02 \pm 1.00) \times 10^{-2}$	$4.69 \pm 0.09 \pm 0.52$
1.877	1.815	2.07	89.9	$(3.68 \pm 0.02 \pm 0.37) \times 10^{-1}$	$4.58 \pm 0.03 \pm 0.46$
	1.813	2.07	49.9	$(4.74 \pm 0.07 \pm 0.52) \times 10^{-1}$	$5.88 \pm 0.09 \pm 0.65$
1.723	1.659	2.00	89.9	$(4.96 \pm 0.02 \pm 0.50) \times 10^{-1}$	$4.20 \pm 0.02 \pm 0.42$
	1.660	2.00	69.9	$(6.35 \pm 0.04 \pm 0.70) \times 10^{-1}$	$5.40 \pm 0.03 \pm 0.59$
	1.659	2.00	49.9	$(7.47 \pm 0.06 \pm 0.82) \times 10^{-1}$	$6.33 \pm 0.05 \pm 0.70$
1.173	1.104	1.72	90.2	$(6.83 \pm 0.04 \pm 0.68) \times 10^{-1}$	$1.17 \pm 0.01 \pm 0.12$
	1.105	1.72	70.2	$1.48 \pm 0.01 \pm 0.16$	$2.55 \pm 0.01 \pm 0.28$
	1.105	1.72	50.2	$3.79 \pm 0.02 \pm 0.42$	$6.53 \pm 0.04 \pm 0.72$

TABLE VI: Differential cross sections for the $\gamma p \rightarrow \pi^+ n$ process followed by the statistical and systematic uncertainties.

E_e (GeV)	E_γ (GeV)	\sqrt{s} (GeV)	$\theta_{c.m.}$ ($^\circ$)	$(\frac{d\sigma}{d\Omega})_{c.m.}$ ($\mu\text{b}/\text{sr}$)	$s^T \frac{d\sigma}{dt}$ ($10^7 \text{ nb} \cdot \text{GeV}^{12}$)
5.614	5.535	3.36	89.8	$(2.55 \pm 0.15 \pm 0.20) \times 10^{-4}$	$0.77 \pm 0.05 \pm 0.06$
	5.537	3.36	100.0	$(2.44 \pm 0.11 \pm 0.19) \times 10^{-4}$	$0.74 \pm 0.03 \pm 0.06$
4.236	4.156	2.95	89.9	$(1.40 \pm 0.03 \pm 0.11) \times 10^{-3}$	$0.94 \pm 0.02 \pm 0.08$
	4.156	2.95	69.7	$(1.79 \pm 0.03 \pm 0.16) \times 10^{-3}$	$1.19 \pm 0.02 \pm 0.11$
	4.156	2.95	100.0	$(1.14 \pm 0.03 \pm 0.09) \times 10^{-3}$	$0.76 \pm 0.02 \pm 0.06$
3.400	3.319	2.67	89.9	$(3.67 \pm 0.05 \pm 0.29) \times 10^{-3}$	$0.78 \pm 0.01 \pm 0.06$
	3.319	2.67	69.7	$(1.78 \pm 0.01 \pm 0.16) \times 10^{-2}$	$3.79 \pm 0.03 \pm 0.34$
	3.321	2.67	49.7	$(1.58 \pm 0.01 \pm 0.14) \times 10^{-1}$	$33.6 \pm 0.18 \pm 3.02$
	3.320	2.67	100.0	$(8.02 \pm 0.11 \pm 0.64) \times 10^{-3}$	$1.71 \pm 0.02 \pm 0.14$
	3.320	2.67	109.9	$(9.51 \pm 0.23 \pm 0.76) \times 10^{-3}$	$2.02 \pm 0.05 \pm 0.16$
2.561	2.481	2.35	90.0	$(5.88 \pm 0.05 \pm 0.47) \times 10^{-2}$	$3.03 \pm 0.03 \pm 0.24$
	2.481	2.35	69.9	$(1.01 \pm 0.01 \pm 0.09) \times 10^{-1}$	$5.21 \pm 0.05 \pm 0.47$
	2.483	2.35	49.8	$(3.29 \pm 0.03 \pm 0.30) \times 10^{-1}$	$17.0 \pm 0.13 \pm 1.53$
1.877	1.801	2.06	89.6	$(2.42 \pm 0.01 \pm 0.19) \times 10^{-1}$	$2.91 \pm 0.01 \pm 0.23$
	1.805	2.07	49.6	$(9.01 \pm 0.04 \pm 0.81) \times 10^{-1}$	$11.0 \pm 0.05 \pm 0.99$
1.723	1.647	1.99	89.6	$(2.89 \pm 0.02 \pm 0.23) \times 10^{-1}$	$2.38 \pm 0.01 \pm 0.19$
	1.648	1.99	69.5	$(5.95 \pm 0.03 \pm 0.54) \times 10^{-1}$	$4.91 \pm 0.03 \pm 0.44$
	1.650	1.99	49.6	$1.15 \pm 0.01 \pm 0.10$	$9.49 \pm 0.05 \pm 0.85$
1.173	1.097	1.71	90.0	$1.35 \pm 0.01 \pm 0.11$	$2.26 \pm 0.01 \pm 0.18$
	1.098	1.72	70.0	$3.13 \pm 0.01 \pm 0.28$	$5.27 \pm 0.02 \pm 0.47$

structure suggested by our data is seen in all three channels of pion photoproduction. The similar broad structure was also seen in the preliminary results from JLab Hall B [61].

B. Scaling at High Energy

Based on the constituent counting rule, the differential cross section $d\sigma/dt$ at a fixed center-of-mass angle

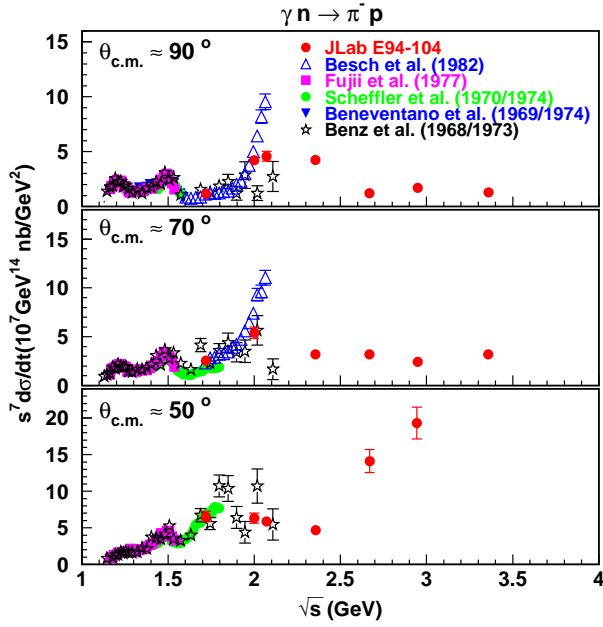


FIG. 14: (Color online). Scaled differential cross section $s^7 \frac{d\sigma}{dt}$ versus center-of-mass energy \sqrt{s} for the $\gamma n \rightarrow \pi^- p$ process from JLab E94-104 and previous world data [44, 58, 59]. The open triangles in the upper panel are averaged from the Besch *et al.* data [58] at $\theta_{c.m.} = 85^\circ$ and 95° , while open triangles in the middle panel are averaged from those at $\theta_{c.m.} = 65^\circ$ and 75° . The Fujii *et al.* and Scheffler *et al.* data [59] in the middle panel were taken at $\theta_{c.m.} = 75^\circ$.

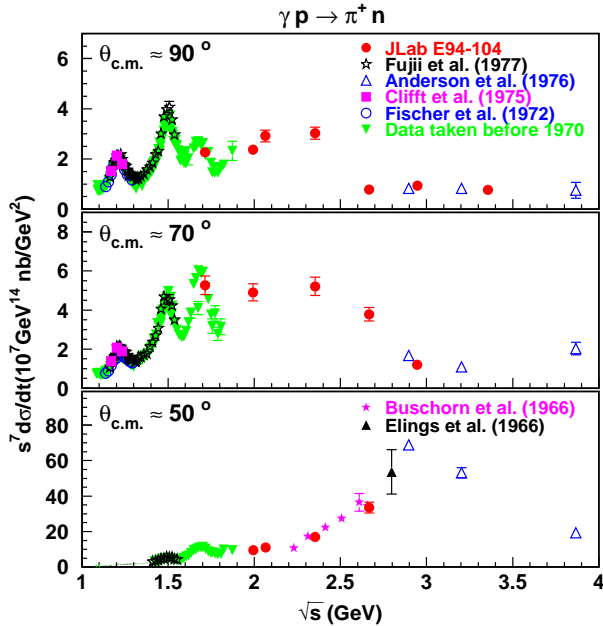


FIG. 15: (Color online). Scaled differential cross section $s^7 \frac{d\sigma}{dt}$ versus center-of-mass energy \sqrt{s} for the $\gamma p \rightarrow \pi^+ n$ process from JLab E94-104 and previous world data [9, 44, 59].

for the $\gamma n \rightarrow \pi^- p$ and $\gamma p \rightarrow \pi^+ n$ processes is predicted to scale as s^{-7} . For both π^- and π^+ photoproduction processes, the data with $\sqrt{s} > 2.7$ GeV at $\theta_{c.m.} = 90^\circ$ and $\sqrt{s} > 3.0$ GeV at $\theta_{c.m.} = 70^\circ$ indicate the scaling behavior of the differential cross section predicted by the constituent counting rule. The fitted power of $\frac{1}{s}$ from the three data points in this region was 6.9 ± 0.2 for the $\gamma n \rightarrow \pi^- p$ process and 7.1 ± 0.2 for the $\gamma p \rightarrow \pi^+ p$ process, consistent with the prediction of 7. This may have some theoretical implications, for example the validity of quark-gluon degrees of freedom and the freezing of the running strong coupling constant at several GeV.

There is no sign of s^{-7} scaling for the data at $\theta_{c.m.} = 50^\circ$ up to center-of-mass energy of 3.0 GeV for the π^- case and 3.9 GeV for the π^+ case. This is not surprising since the deuteron photodisintegration data [7, 8, 28] at forward angles do not scale at as low energies as those at 90° . The deuteron photodisintegration data at $\theta_{c.m.} = 53^\circ$ seem to scale when the photon energy is greater than 3 GeV while the data at $\theta_{c.m.} = 90^\circ$ scale when the photon energy is greater than 1 GeV. The corresponding center-of-mass energies are 3.8 GeV and 2.7 GeV respectively.

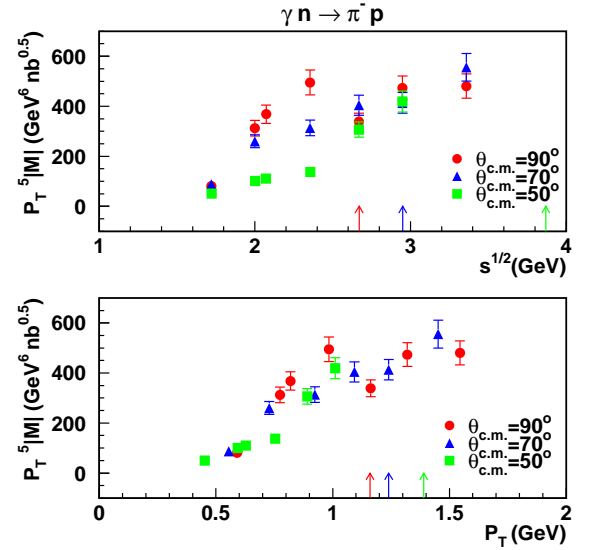


FIG. 16: (Color online). Scaled amplitude $P_T^5 |M|$ versus center-of-mass energy \sqrt{s} and transverse momentum P_T for the $\gamma n \rightarrow \pi^- p$ process. All the data points came from JLab E94-104. The arrows indicate the position below which the data do not scale for either π^+ or π^- photoproduction.

The scaled invariant amplitude $P_T^5 |M|$ is plotted in Figure 16 and Figure 17 against center-of-mass energy \sqrt{s} and transverse momentum P_T , similar to that performed for neutral pion photoproduction on the deuteron [62]. The invariant amplitude M was calculated from the differential cross section by using

$$|M| = 4(s - m_N^2) \sqrt{\pi \frac{d\sigma}{dt}(\gamma N \rightarrow \pi N)}, \quad (8)$$

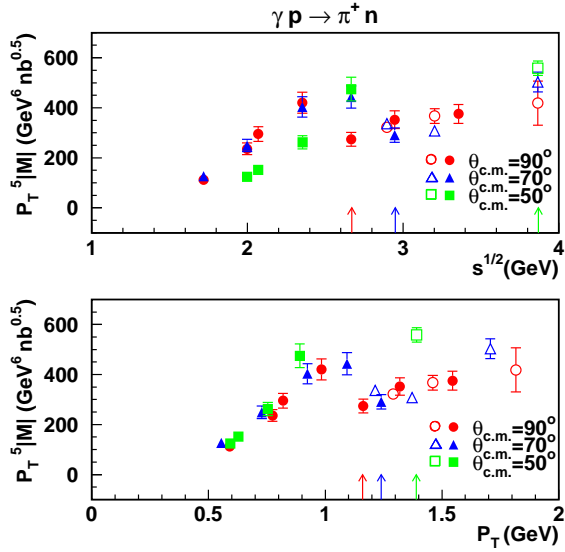


FIG. 17: (Color online). Scaled amplitude $P_T^5 |M|$ versus center-of-mass energy \sqrt{s} and transverse momentum P_T for the $\gamma p \rightarrow \pi^+ n$ process. The data points in solid circles came from JLab E94-104, while those in open triangles are SLAC data [9]. The arrows indicate the position below which the data do not scale for either π^+ or π^- photoproduction.

and the transverse momentum was calculated by using $P_T = |\vec{p}_\pi| \sin \theta_\pi$ from the pion momentum \vec{p}_π and scattering angle θ_π . The scaled amplitude $P_T^5 |M|$ is plotted here for the $\gamma N \rightarrow \pi^\pm N$ process, while $P_T^{11} |M|$ was plotted in reference [62] for the $\gamma d \rightarrow \pi^0 d$ process. The scaling power of P_T can be estimated by dimensional counting. Since the arrows in different colors (indicating the possible onset of scaling for different angles) are closer in terms of transverse momentum than in terms of the center-of-mass energy, the transverse momentum may be a better choice to describe the scaling onset than the center-of-mass energy, which was also stated previously [25, 63]. The photoproduction data seem to reach the scaling region when the transverse momentum is around 1.2 GeV/c. As a comparison, the deuteron photodisintegration data start to exhibit scaling when proton transverse momentum ranges from 1.0 to 1.3 GeV/c at proton center-of-mass angle between 30° to 150° , except that the proton transverse momentum threshold ranges from 0.6 to 0.7 GeV/c at center-of-mass angle of 45° , 135° and 145° [8]. Another interesting observation is that the scaled amplitude has much less dependence on center-of-mass angle than do the scaled cross sections.

C. Possible Substructure of Scaling

As shown in Figure 18 [19], one can see some substructure of the global scaling for both processes: the point around 3.0 GeV is higher than those at 2.7 GeV and 3.4 GeV. This might be a hint of possible oscillations

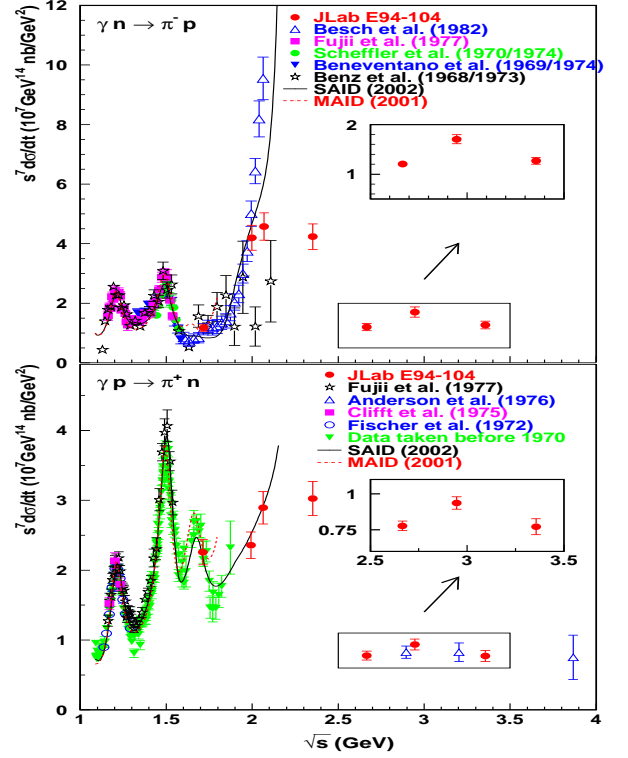


FIG. 18: (Color online). Scaled differential cross section $s^7 \frac{d\sigma}{dt}$ versus center-of-mass energy \sqrt{s} for the $\gamma n \rightarrow \pi^- p$ process (upper panel) and $\gamma p \rightarrow \pi^+ n$ process (lower panel) at $\theta_{c.m.} = 90^\circ$ from JLab E94-104 and previous world data [9, 44, 58, 59]. The error bars in the insets include only point-to-point uncertainties to highlight the possible substructure of scaling. The solid line was obtained from the recent partial-wave analysis of the single pion photoproduction data up to $E_\gamma = 2$ GeV [66], while the dashed line was obtained from the MAID analysis up to $E_\gamma = 1.25$ GeV [67]

around the scaling value, similar to what was observed in the pp elastic scattering data [14]. Future measurements planned at JLab [64], with finer binning in beam energy, are essential for the confirmation of such oscillatory scaling behavior.

The substructure or the possible oscillatory scaling behavior in pion photoproduction may arise from the same mechanism as in the case of pp scattering, i.e. the interference between the long-distance (due to Landshoff diagrams) amplitude and short-distance amplitude [35], or the interference between resonances with a pQCD background [36]. But it may also be due to other mechanisms, such as high energy resonances around 3 GeV [57], the interference between the amplitudes associated with different helicity changes based on the generalized counting rule [37], or the breaking of the local quark-hadron duality above the resonance region [40].

The generalized constituent counting rule [37] was derived for hard exclusive processes involving parton orbital momentum and hadron helicity flip. It predicts that $M(\gamma N_\uparrow \rightarrow \pi N_\downarrow) \sim s^{-3}$ and $d\sigma/dt(\gamma N_\uparrow \rightarrow \pi N_\downarrow) \sim s^{-8}$

for the helicity-flip case, while $M(\gamma N_{\uparrow} \rightarrow \pi N_{\uparrow}) \sim s^{-5/2}$ and $d\sigma/dt(\gamma N_{\uparrow} \rightarrow \pi N_{\uparrow}) \sim s^{-7}$ for the helicity conserving case. The interference between the amplitudes with different helicity changes offers a new mechanism to explain the possible oscillations around the scaling value. But the resulting oscillation pattern should be different from that caused by interference between the short-distance and long-distance amplitudes. At sufficiently high energy, the helicity-flip amplitude will become negligible while the long-distance amplitude will be larger than the traditional scaling one (the helicity conserving amplitude or short-distance amplitude) due to the different energy dependences.

The locality of quark-hadron duality means that the local averages of physical variables measured in the resonance region are equal to those measured in the deep-inelastic or scaling region. The locality of quark-hadron duality can be realized in a simple model of a composite system with two spinless charged constituents described by harmonic oscillator wave functions with principal quantum number N and orbital angular momentum $L (\leq N)$. The destructive interference between the high density of overlapping resonances leads to the smooth scaling behavior at high energies. But for medium energies, the locality of quark-hadron duality may break down and a sizable oscillation around the scaling value may appear above the resonance region due to the orbital angular momentum dependence of the resonances [40]. In this mechanism, the energy increase reduces the oscillation amplitude, and the Q^2 dependence may be nontrivial. If a subset of resonances are relatively suppressed at large Q^2 , there will be significant shifts in the position and magnitude of oscillations. The deviation pattern produced by the resonance degeneracy breaking requires no simple periodicity. The experimental data can thus distinguish this mechanism from others.

D. Cross Section Enhancement around 2.2 GeV

Another interesting feature of the differential cross section is an apparent enhancement with a sharp drop for both channels of the charged pion photoproduction at $\theta_{c.m.} = 90^\circ$, at a center-of-mass energy ranging approximately from 1.8 to 2.5 GeV, as shown in Figure 18. Note that it is the scaled cross sections $s^7 d\sigma/dt$ that are plotted. The drop is even faster in terms of non-scaled cross section. A similar cross section enhancement was also observed in neutral pion photoproduction. But the enhancement patterns are different for the kinematics at $\theta_{c.m.} = 70^\circ$ and $\theta_{c.m.} = 50^\circ$.

Some speculation can be made about the enhancement. It might be due to the known baryon resonances around this energy, for example $G_{17}(2190)$, $H_{17}(2220)$ and $G_{19}(2250)$ [57], just as is the case at lower energies. It might relate to some missing resonances [65], which were predicted by the constituent quark model but have not been seen experimentally. The value of center-of-

mass energy hints that the enhancement might be associated with the strangeness production threshold, which is around 2 GeV to produce a ϕ meson of mass 1 GeV. The resonances at strangeness and charm production thresholds were assumed in an approach to explain the strong spin-spin correlation and oscillatory scaling in elastic pp scattering [36]. It is worthwhile to mention that a broad bump near 2.2 GeV appears in the π^-p total cross section, while it is not clear in π^-p elastic cross section [57].

E. Exclusive Charged Pion Ratio

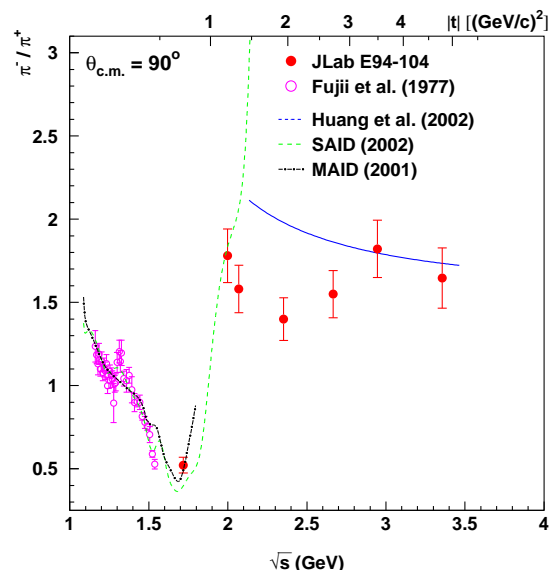


FIG. 19: (Color online). Exclusive charged pion ratio $\frac{d\sigma/dt(\gamma n \rightarrow \pi^- p)}{d\sigma/dt(\gamma p \rightarrow \pi^+ n)}$ versus center-of-mass energy \sqrt{s} and momentum transfer square $|t|$ at pion center-of-mass angle $\theta_{c.m.} = 90^\circ$ from JLab E94-104 and previous world data [59], together with the SAID [66], MAID [67] and one-hard-gluon-exchange calculation [42, 43].

One can form the exclusive charged pion ratio $\frac{d\sigma/dt(\gamma n \rightarrow \pi^- p)}{d\sigma/dt(\gamma p \rightarrow \pi^+ n)}$ based on the E94-104 data. As shown in Figure 19, the exclusive charged pion ratio has some oscillations at low energies due to the isospin dependence of the resonances, which can be described by the SAID [66] and MAID [67] calculations available at low energies. The big jump around 2 GeV might be associated with the isospin-dependent resonances nearby, or with the strangeness production threshold (around 2 GeV for ϕ production). The lowest order (leading-twist) calculation based on one-hard-gluon-exchange diagrams [42, 43], which is only valid at high energies, predicts a smooth and simple behavior of $\frac{d\sigma/dt(\gamma n \rightarrow \pi^- p)}{d\sigma/dt(\gamma p \rightarrow \pi^+ n)} \simeq \left(\frac{ue_d + se_u}{ue_u + se_d}\right)^2$ after the nonperturbative components represented by the form factors are divided out in the ratio. The theoretical prediction seems to agree with the $\theta_{c.m.} = 90^\circ$ data at the two highest energies.

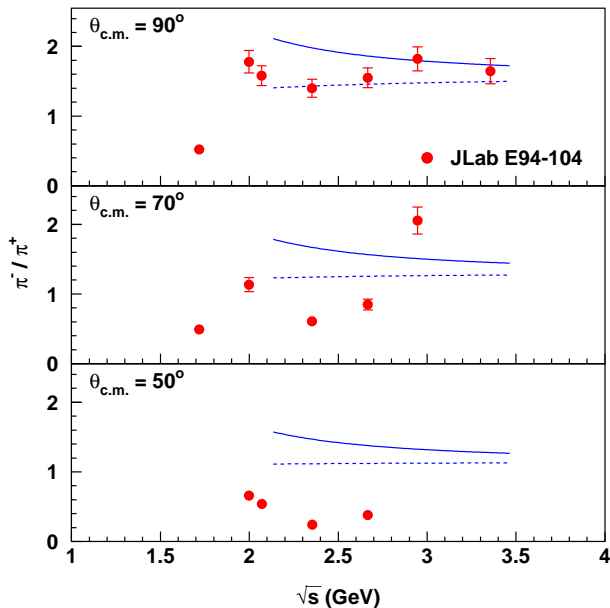


FIG. 20: (Color online). Exclusive charged pion ratio $\frac{d\sigma/dt(\gamma n \rightarrow \pi^- p)}{d\sigma/dt(\gamma p \rightarrow \pi^+ p)}$ versus center-of-mass energy \sqrt{s} at different pion center-of-mass angles from JLab E94-104. The solid curve is calculated by using Equation 4, while the dashed one considers the nucleon mass by using Equation 9.

The exclusive charged pion ratio was also calculated to higher orders (twist-2 and twist-3) within the handbag mechanism considering both quark helicity flip and non-flip [68]. The more precise approach led to the same result as the leading-twist prediction when $|C_2^P| \gg |C_3^P|$. The invariant functions $|C_i^P|$ ($i = 1, 4$) are the coefficients for the four gauge invariant covariants into which the meson photoproduction amplitudes can be decomposed. Both $|C_2^P|$ and $|C_3^P|$ contribute only to the quark helicity conserving amplitudes while $|C_1^P|$ and $|C_4^P|$ generate quark helicity flips. The charged pion ratio will become infinity at large s if $|C_3^P|$ is dominant, which is clearly not supported by our data.

The calculation was for massless particle. The effects due to nucleon mass may be important at an energy scale of few GeV, as estimated by the difference between the solid and dashed curves in Figure 20. The calculation shown by the dashed curve considers the nucleon mass by using the identification [69] of the Mandelstam variables with the experimental ones ($s_{\text{exp}}, t_{\text{exp}}, u_{\text{exp}}$)

$$s = s_{\text{exp}} - m_p^2; t = t_{\text{exp}}; u = u_{\text{exp}} - m_p^2, \quad (9)$$

so that $s+t+u \sim 0$. Figure 20 also shows that the agreement at forward angles is not as good as the case at 90° , which might be related to the relatively lower momentum transfer. Measurements at higher energies are necessary to fully check the theoretical approach, though the current comparison between prediction and data seems to

suggest that the handbag mechanism is at work for the pion photoproduction processes with dominant quark helicity non-flip amplitudes and $|C_2^P| \gg |C_3^P|$.

VI. OUTLOOK

As mentioned above, a new proposal E02-012 [64] has been approved in JLab Hall A to measure the $\gamma n \rightarrow \pi^- p$ process with deuterium and carbon targets, as well as the $\gamma p \rightarrow \pi^+ n$ process with a hydrogen target. With very fine steps in center-of-mass energy, approximately 0.07 GeV, the new experiment will be able to elucidate more details about the possible substructure of the scaling behavior. In addition, the nuclear transparency of carbon in the pion photoproduction process will be measured for the first time. This should enable us to test some theoretical predictions such as the nuclear filtering effect and color transparency. The latter was suggested by the helium transparency measurement in E94-104 [20].

Since the cross section decreases relatively slowly as energy increases, the measurements for single pion photoproduction processes can be greatly extended with the JLab 12 GeV upgrade. Since the charm production threshold will be crossed, one would be able to investigate the resonance at this threshold that was assumed in an approach to explain the anomalies in pp scattering [36]. In addition, one would be able to further test the scaling and charged pion ratio predictions, especially at forward angles.

VII. ACKNOWLEDGMENTS

We acknowledge the outstanding support of JLab Hall A technical staff and Accelerator Division in accomplishing this experiment. We thank R. B. Wiringa and H. Arenhövel for calculating the momentum distribution of the neutron in the deuterium target. We thank Z. Chai for providing the code to apply R-function cut on acceptance. We also thank S. Brodsky, T. W. Donnelly, H. W. Huang, P. Jain, P. Kroll, J. Ralston, C. D. Roberts, P. Rossi and G. de Teramond for helpful discussions. This work was supported in part by the U. S. Department of Energy, DOE/EPSCoR, the U. S. National Science Foundation, the Ministero dell'Università e della Ricerca Scientifica e Tecnologica (Murst), the French Commissariat à l'Énergie Atomique, Centre National de la Recherche Scientifique (CNRS) and the Italian Istituto Nazionale di Fisica Nucleare (INFN). This work was supported by DOE contract DE-AC05-84ER40150 under which the Southeastern Universities Research Association (SURA) operates the Thomas Jefferson National Accelerator Facility.

-
- [1] S. J. Brodsky and G. R. Farrar, Phys. Rev. Lett. **31**, 1153 (1973).
- [2] S. J. Brodsky and G. R. Farrar, Phys. Rev. D **11**, 1309 (1975).
- [3] V. A. Matveev, R. M. Muradyan and A. N. Tavkhelidze, Nuovo Cimento Lett. **7**, 719 (1973).
- [4] G. P. Lepage and S. J. Brodsky, Phys. Rev. D **22**, 2157 (1980).
- [5] P. V. Landshoff and J. C. Polkinghorne, Phys. Lett. B **44**, 293 (1973).
- [6] C. White *et al.*, Phys. Rev. D **49**, 58 (1994).
- [7] R. Gilman and F. Gross, J. Phys. G **28**, R37 (2002); E. C. Schulte *et al.*, Phys. Rev. Lett. **87**, 102302 (2001); C. Bochna *et al.*, Phys. Rev. Lett. **81**, 4576 (1998); C. E. Carlson *et al.*, Annu. Rev. Nucl. Part. Sci. **47**, 395 (1997); S. J. Freedman *et al.*, Phys. Rev. C **48**, 1864 (1993); J. E. Belz *et al.*, Phys. Rev. Lett. **74**, 646 (1995); J. Napolitano *et al.*, Phys. Rev. Lett. **61**, 2530 (1988).
- [8] M. Mirazita *et al.* Phys. Rev. C **70**, 014005 (2004); P. Rossi *et al.*, hep-ph/0405207, (2004).
- [9] R. L. Anderson *et al.*, Phys. Rev. D **14**, 679 (1976); Phys. Rev. Lett. **30**, 627 (1973).
- [10] S. J. Brodsky and G. P. Lepage, Phys. Rev. D **24**, 2848 (1981).
- [11] K. Wijesooriya *et al.*, Phys. Rev. Lett. **86**, 2975 (2001).
- [12] K. Wijesooriya *et al.*, Phys. Rev. C **66**, 034614 (2002).
- [13] E. A. Crosbie *et al.*, Phys. Rev. D **23**, 600 (1981); D. G. Crabb *et al.*, Phys. Rev. Lett. **41**, 1257 (1978).
- [14] A. W. Hendry, Phys. Rev. D **10**, 2300 (1974).
- [15] A. S. Carroll *et al.*, Phys. Rev. Lett. **61**, 1698 (1988); I. Mardor *et al.*, Phys. Rev. Lett. **81**, 5085 (1998); A. Leksanov *et al.*, Phys. Rev. Lett. **87**, 212301 (2001).
- [16] T. Gousset, B. Pire and J. P. Ralston, Phys. Rev. D **53**, 1202 (1996).
- [17] A. V. Belitsky, X. Ji, and F. Yuan, Phys. Rev. Lett. **91**, 092003 (2003).
- [18] JLab experiment E94-104, spokespersons: H. Gao and R. J. Holt, (1994).
- [19] L. Y. Zhu *et al.*, Phys. Rev. Lett. **91**, 022003 (2003).
- [20] D. Dutta *et al.*, Phys. Rev. C **68**, 021001(R) (2003); H. Gao, R. J. Holt, and V. R. Pandharipande, Phys. Rev. C **54**, 2779 (1996).
- [21] S. J. Brodsky, S. Menke, C. Merino and J. Rathsman, Phys. Rev. D **67**, 055008 (2003).
- [22] P. V. Landshoff, Phys. Rev. D **10**, 1024 (1974).
- [23] J. Polchinski and M. J. Strassler, Phys. Rev. Lett. **88**, 031601 (2002).
- [24] V. Yu. Grishina *et al.*, Eur. Phys. J. A **10**, 355 (2001). V. Yu. Grishina *et al.*, Eur. Phys. J. A **19**, 117 (2004).
- [25] S. J. Brodsky and J. R. Hiller, Phys. Rev. C **28**, 475 (1983).
- [26] A. E. L. Dieperink *et al.*, Phys. Lett. B **456**, 9 (1999).
- [27] L. L. Frankfurt, G. A. Miller, M. M. Sargsian and M. I. Strikman, Phys. Rev. Lett. **84**, 3045 (2000).
- [28] E. C. Schulte, Ph.D. Thesis, University of Illinois at Urbana-Champaign, (2002).
- [29] E. C. Schulte *et al.*, Phys. Rev. C **66**, 042201 (2002).
- [30] N. Isgur and C. H. L. Smith, Phys. Rev. Lett. **52**, 1080 (1984).
- [31] J. P. Ralston and P. Jain, hep-ph/0207129, (2002); J. P. Ralston, R. V. Buniy and P. Jain, hep-ph/0206063, (2002)
- [32] G. A. Miller and M. R. Frank, Phys. Rev. C **65**, 065205 (2002).
- [33] M. K. Jones *et al.*, Phys. Rev. Lett. **84**, 1398 (2000); O. Gayou *et al.*, Phys. Rev. C **64**, 038202 (2001); O. Gayou *et al.*, Phys. Rev. Lett. **88**, 092301 (2002).
- [34] S.J. Brodsky, J.R. Hiller, D.S. Hwang and V.A. Karmanov, Phys. Rev. D **69**, 076001 (2004).
- [35] J. P. Ralston and B. Pire, Phys. Rev. Lett. **61**, 1823 (1988).
- [36] S. J. Brodsky, and G. F. de Teramond, Phys. Rev. Lett. **60**, 1924 (1988).
- [37] X. Ji, J. P. Ma and F. Yuan, Phys. Rev. Lett. **90**, 241601 (2003).
- [38] S.J. Brodsky, G.F. de Teramond, Phys. Lett. B **582**, 211 (2004).
- [39] D. Dutta, H. Gao, hep-ph/0411267, (2004).
- [40] Q. Zhao and F. E. Close, Phys. Rev. Lett. **91**, 022004 (2003).
- [41] E. D. Bloom and F. J. Gilman, Phys. Rev. D **4**, 2901 (1971).
- [42] H. W. Huang, private communication.
- [43] H. W. Huang and P. Kroll, Eur. Phys. J. C **17**, 423 (2000); P. Kroll, hep-ph/0207118, (2002); A. Afanasev, C. E. Carlson, and C. Wahlquist, Phys. Lett. B **398**, 393 (1997).
- [44] HEPDATA: REACTION DATA Database, <http://durpdg.dur.ac.uk/hepdata/reac.html>; H. Genzel, P. Joos, and W. Pfeil, *Photoproduction of Elementary Particles*, Group I Volume 8 of Numerical Data and Functional Relationships in Science and Technology, edited by K.-H. Hellwege, Springer-Verlag Press, Berlin, (1973).
- [45] J. Alcorn *et al.*, Nucl. Instrum. Methods A **522**, 294 (2004).
- [46] C. W. Leemann, D. R. Douglas, and G. A. Krafft, Ann. Rev. Nucl. Part. Sci. **51**, 413 (2001).
- [47] <http://www.physics.odu.edu/~ulmer/mceep/mceep.html>
- [48] J. L. Matthews and R. O. Owens, Nucl. Instrum. Methods **111**, 157 (1973).
- [49] D. G. Meekins, Ph.D. Thesis, College of William and Mary, (1998); <http://www.jlab.org/~meekins/gammapcode.tgz>.
- [50] J. L. Matthews, D. J. S. Findlay, and R. O. Owens, Nucl. Instrum. Methods **180**, 573 (1981).
- [51] M. Rvachev, JLab Technical Note, JLAB-TN-01-055 (2001).
- [52] Z. Chai, Ph.D. Thesis, Massachusetts Institute of Technology, (2003).
- [53] J. Arrington, <http://www.jlab.org/~johna/>.
- [54] J. Arrington, private communication.
- [55] K. Garrow *et al.*, Phys. Rev. C **66**, 044613 (2002).
- [56] L. L. Frankfurt *et al.*, Z. Phys. A **352**, 97 (1995).
- [57] K. Hagiwara *et al.*, Phys. Rev. D **66**, 010001 (2002); <http://pdg.lbl.gov/>.
- [58] H.-J. Besch *et al.*, Z. Phys. C **16**, 1 (1982).
- [59] Fujii *et al.*, Nucl. Phys. B **120**, 396 (1977); Scheffler *et al.*, Nucl. Phys. B **75**, 125 (1974); Phys. Rev. Lett. **24**, 952 (1970); Beneventano *et al.*, Nuovo Cimento **19A**, 529 (1974); Nuovo Cimento Lett. **1**, 113 (1969); Benz *et al.*, Nucl. Phys. B **65**, 158 (1973); Hilpert *et al.*, Nucl.

- Phys. B **8**, 535 (1968); Clift *et al.*, Phys. Rev. Lett. **33**, 1500 (1975); Fischer *et al.*, Z. Phys. C **253**, 38 (1972); Buschorn *et al.*, Phys. Rev. Lett. **17**, 1027 (1966); Elings *et al.*, Phys. Rev. Lett. **16**, 474 (1966).
- [60] G. R. Farrar, K. Huleihel, and H. Zhang, Nucl. Phys. B **349**, 655 (1991).
- [61] R. Schumacher, private communication.
- [62] S. J. Brodsky, J. R. Hiller, Chueng-Ryong Ji, and G. A. Miller, Phys. Rev. C **64**, 055204 (2001).
- [63] C. E. Calson, J. R. Hiller and R. J. Holt, Ann. Rev. Nucl. Part. Sci. **47**, 395 (1997).
- [64] JLab experiment E02-010, spokespersons: D. Dutta, H. Gao, and R. J. Holt, (2002).
- [65] S. Capstick, Phys. Rev. D **46**, 2864 (1992); S. Capstick and W. Roberts, Phys. Rev. D **49**, 4570 (1994).
- [66] I. I. Strakovsky, private communication; R. A. Arndt, W. J. Briscoe, I. I. Strakovsky, and R. L. Workman, Phys. Rev. C **66**, 055213 (2002); <http://gwdac.phys.gwu.edu/>.
- [67] I. I. Strakovsky, private communication; S. S. Kamalov, S. N. Yang, D. Drechsel, O. Hanstein and L. Tiator, Phys. Rev. C **64**, 032201(R) (2001)(a dynamical model); D. Drechsel, *et al.*, Nucl. Phys. A **645**, 145 (1999)(a unitary isobar model); <http://www.kph.uni-mainz.de/MAID/>. MAID2001 refers to the Nov. 2001 version of the MAID solution from S. S. Kamalov.
- [68] H. W. Huang, R. Jakob, P. Kroll, and K. Passek-Kumerički, Eur. Phys. J. C **33**, 91 (2004).
- [69] M. Diehl, T. Feldmann, H. W. Huang, and P. Kroll, Phys. Rev. D **67**, 037502 (2003).